Journal of Sound and Vibration 494 (2020) 115902

Contents lists available at ScienceDirect

Journal of Sound and Vibration

journal homepage: www.elsevier.com/locate/jsv

Robust reconstruction of scattering surfaces using a linear microphone array

G. Dolcetti [a,*], M. Alkmim [b,c], J. Cuenca [b], L. De Ryck [b], A. Krynkin [d]

[a] The University of Sheffield, Department of Civil and Structural Engineering, Sheffield, United Kingdom
[b] Siemens Digital Industries Software, Interleuvenlaan 68, Leuven B-3001, Belgium
[c] KU Leuven, Department of Mechanical Engineering, Celestijnenlaan 300 B, Leuven, B-3001, Belgium
[d] The University of Sheffield, Department of Mechanical Engineering, Sheffield, United Kingdom

ARTICLE INFO

Article history:
Received 30 July 2020
Revised 26 November 2020
Accepted 4 December 2020
Available online 5 December 2020

Keywords:
Scattering
Surface inversion
Microphone array

ABSTRACT

The analysis of sound scattered by a rough surface and measured by multiple microphones positioned in the far field yields an estimate of the unknown scattering surface profile. Expanding from previous work, the approach used in this paper is based on an expansion and linearization of the Kirchhoff integral equation, and applies to a low density of receivers. Here, the original algorithm is modified in order to reduce the measurement bias, and extended to broadband signals to over-constrain the problem and improve its robustness. The improved method is rigorously assessed alongside the original algorithm and its small perturbation version, for a two-dimensional geometry and for scattering surfaces with a spatial power-function spectrum. The impact of the measurement setup and surface characteristics on the reconstruction uncertainty are evaluated by means of numerical simulations. Additional experimental data obtained for three known surface profiles reveal the impact of noise and measurement uncertainties. The optimal measurement configuration requires a trade-off between resolution (higher at high frequencies), and robustness (higher at low frequencies). This limit is overcome at least partially by the proposed multiple-frequency extension. The resulting measured uncertainties were close to the theoretical expectation of approximately 2% of the acoustic wavelength.

1. Introduction

Measurements of the shape of the interface between two media are ubiquitous across engineering and geophysics, including applications such as non-destructive testing, microscopy, and remote sensing. In this paper the focus is on rough surfaces, i.e., smooth perturbations of an otherwise flat plane. Examples include the ocean bottom [1], sea waves [2,3], or river surfaces [4,5]. The accurate characterization of these surfaces is key to effective flood prevention and monitoring of geophysical processes. One way to measure them is to observe the behavior of a wave field as it interacts with the interface. Specifically, if transmission through the interface can be neglected (this is the case, for example, of high frequency sound

* Corresponding author.
E-mail addresses: g.dolcetti@sheffield.ac.uk (G. Dolcetti), mansour.alkmim@siemens.com (M. Alkmim), jacques.cuenca@siemens.com (J. Cuenca), laurent.deryck@siemens.com (L. De Ryck), a.krynkin@sheffield.ac.uk (A. Krynkin).

https://doi.org/10.1016/j.jsv.2020.115902
0022-460X/

on the water-air or air-water interface), the surface shape can be estimated based on a model of scattering and a measurement of the scattered signal by a number of sensors distributed in space. Surface reconstruction techniques based on this principle have been developed for optical [6,7], electromagnetic [8–13], elastic [14], and acoustic [15–17] wave signals.

Uniqueness of the solution of the inverse surface scattering problem is discussed in [9,18–20]. Surface reconstruction techniques include methods that apply to time-domain data [3,21,22], methods that identify the surface location from the maxima or minima of an imaging function mapped in all spatial dimensions [6,23–25], and methods that yield directly the surface function (or its projection on a certain basis). The latter is achieved either by minimizing the difference between the observed and predicted field variable distribution (optimization problem) [10,20,26–28], or by inverting the boundary integral equations that define the forward problem, i.e., that of calculating the scattered field for a given scattering interface geometry. The advantage of these latter approaches is that they do not require, in principle, a prior parametrization of the surface. On the other hand, one needs to determine the unknown distributions of two quantities (the surface shape and the field variable on all boundaries, including the interface). This can be achieved iteratively [12,13,29,30] or directly [31,32]. An alternative is to use an approximate expression to determine the field at the surface, thus reducing the number of unknowns. Approximations that can be used include the Kirchhoff approximation [8,16], Rytov approximation [33], small perturbation expansion [11,34], and Milder's operator expansion [15]. This simplifies the inversion, although it may yield a loss of accuracy in the conditions where the approximations fail, typically for surfaces with high curvature or in the presence of shadowing or multiple reflections.

Starting from the Kirchhoff approximation of the scattering integral equations, Krynkin et al. [17] formulated the acoustic scattering forward problem for a rigid surface in the form of a matrix product. This enabled a straightforward reconstruction of the surface shape after a singular value decomposition (SVD) of the transfer matrix, and its subsequent inversion. A similar approach is commonly used for some source imaging problems [35]. There, the method has been extended to underdetermined problems [36], where the number of unknown elementary sources is greater than the number of sensors. Similarly, the surface reconstruction method introduced in [17] applies to sparse sensors arrays, where the number of receivers is smaller than the number of points that discretize the surface. This makes the method a strong candidate for a variety of applications, especially in acoustics where physical dimensions and cost of the microphones limit the achievable density of sensors. The approach introduced in [17] was validated experimentally [37], for two examples of rough surface and with a single microphone that was scanned along an arch. With the exception of [16] (tested on periodic gratings), and [3] (tested on non-periodic water waves), most other surface reconstruction techniques lack an experimental validation. As a result, little is known about their performance in a realistic measurement environment. Additionally, the influence of the sensors array geometry and surface parameters on the measurement uncertainties, and the statistics of the reconstruction error, have not been thoroughly investigated.

The present work aims to bridge these gaps using new numerical and experimental results obtained with approaches derived from the method presented in [17]. Here, this method is denoted as the short array (SA) method. Synthetic data of the sound field scattered by a large number of random rough surfaces with a power-function spatial spectrum are generated with an acoustic model based on the Kirchhoff approximation, assuming constant surface elevation in one direction. The synthetic data are then analyzed with the SA method, to reconstruct the profile of each surface. The SA method is also based on the Kirchhoff approximation, but the inverse model equations include additional approximations and expansions. This avoids the 'inverse crime' consisting in using the same model for the forward and inverse problem, except when this is required for a self-consistency test. The analysis of numerical data enables to inspect the statistical distribution of the reconstruction error for a large collection of surfaces with similar properties, and for various characteristics of the measurement setup (signal frequency, sensors height and separation) and surface parameters (roughness vertical and horizontal scales, spectrum slope). Three error metrics are found necessary for a compact and consistent representation of the error distribution. The numerical analysis is complemented by experimental tests on three rough surfaces, obtained with an array of 34 microphones. The experimental data, recorded at multiple frequencies using a broadband random excitation, serve two purposes: they validate (within the range of the tests) the numerical analysis based on a Kirchhoff approximation model, and they highlight a number of issues relevant for the application, namely the effect of phase uncertainty and noise, and the robustness and accuracy of single measurements.

Two modifications of the SA method are newly introduced in this work, and tested alongside the SA method. The first (SA0 method) is a preconditioning of the linearized problem which fixes an otherwise inconsistent use of the Tikhonov regularization. The second (SP method) is an alternative derivation based on a small perturbation expansion of the scattering integral equations. A further multiple frequency extension to all methods is introduced, based on the following idea: since the shape of a scattering surface is independent of the frequency of excitation of the incident field, information about the scattered field at different frequencies can be combined to impose additional constraints on the inversion. This had been achieved previously for other methods, by sequentially introducing data at increasing frequencies to improve an initial coarse reconstruction at a low frequency [20,27,28,38]. Here, the additional information is combined into a single problem, which is solved simultaneously at all frequencies. A somehow similar approach was recently proposed for the related problem of scattering from finite-size volumetric scatterers [39]. In its application to the SA surface reconstruction method, the most noticeable property of the multiple frequency extension is its capability to transform the forward linear system from underdetermined to overdetermined, with consequences on the accuracy and stability of the inverse solution.

This work is organized as follows: The statement of the forward problem and the derivation of the three inversion methods and their multiple-frequency extension are presented in Section 2; the results of the numerical analysis based on syn-

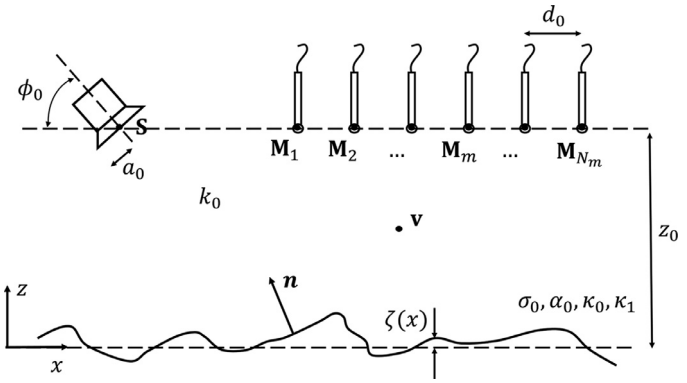

Fig. 1. Schematic representation of the surface scattering problem geometry, and characteristic parameters: acoustic wavenumber k_0, source inclination angle ϕ_0, equivalent piston radius a_0, microphone array separation d_0 and height z_0, surface standard deviation σ_0, spectrum slope α_0, and large-scale, κ_0, and short-scale, κ_1, cut-off wavenumbers. The rough surface is described by the function $z = \zeta(x)$, with normal vector $\mathbf{n}$.

thetic scattered field data are presented in Section 3; the synthetic data was calculated based on a form of the Kirchhoff approximation equation, which is derived in Appendix A for scattering surfaces with constant elevation in one direction; experimental surface reconstruction results are reported in Section 4; numerical and experimental results are compared and discussed in Section 5; and the conclusions of the study can be found in Section 6.

2. Fundamentals of the method

All surface inversion methods discussed here have the so-called Kirchhoff approximation [40] as a starting point. This approximation is valid when the scattering surface is sufficiently smooth, i.e., $2kr_c \sin^3\phi > 1$, where $k = 2\pi/\lambda$ is the acoustic wavenumber, $\lambda = c/f$ is the wavelength, f is the frequency, c is the speed of sound, r_c is the surface local radius of curvature, and ϕ is the angle of incidence of sound measured from the horizontal. Here it is assumed that sound propagates in air, with $c = 340$ m s^{-1}. The acoustic signal is harmonic in time with frequency f, or can be represented as a linear combination of harmonic signals. In the latter case, the theory applies to each component independently. The Kirchhoff approximation consists in evaluating the acoustic field on the rough surface at each point, considering only the locally tangent flat plane. A general form of the resulting integral equation valid for an acoustically rigid surface of the form $z = \zeta(x, y)$ is reported in the Appendix A. Different boundary conditions at the surface could lead to qualitatively similar results [41, p. 228], but their implementation is beyond the scope of this work.

In a realistic three-dimensional case, ζ varies along x and y, and the microphones are distributed in three dimensions in space. To reduce the computational effort and the number of parameters that describe the system, here the problem was simplified as follows: (i) the elevation of the rough surface ζ was assumed to vary only in the x-direction, i.e., $\zeta = \zeta(x)$; (ii) the width of the surface in the y direction was assumed to be infinite; (iii) the source and all microphones were assumed to lie on the same plane $y = 0$, normal to the surface. These conditions enable a stationary phase expansion within the Kirchhoff approximation integral equation, hence allowing to integrate along y, independently of the surface shape. Details of the calculations are reported in the Appendix.

With such premise, sound is considered to be emitted by an acoustic source with co-ordinate vector $\mathbf{S} = (x_s, z_s)$, and scattered at a rough surface $z = \zeta(x)$, where the plane $z = 0$ coincides with the average of $\zeta(x)$ over x, $\bar{\zeta}(x) = 0$. The scattered sound field is recorded by an array of N_m microphones, with the co-ordinates of the mth microphone indicated by $\mathbf{M}_m = (x_m, z_m)$, as depicted in Fig. 1. The source is approximated as a point source with a directivity pattern $D(\theta(\mathbf{v} - \mathbf{S}))$, where $\theta(\mathbf{v} - \mathbf{S})$ is the angle between vector $\mathbf{v} - \mathbf{S}$ and the axis of the transducer, and $\mathbf{v}$ is a generic location in space. $D(\theta(\mathbf{M}_m - \mathbf{S}))$ is assumed to be small at the microphone locations, therefore the direct field is neglected. The distance from $\mathbf{v} = (x_v, z_v)$ to a point at the intersection between the surface and the plane $y = 0$, $\boldsymbol{\rho} = (x, \zeta(x))$, is

$$R(\mathbf{v}, \boldsymbol{\rho}) = |\mathbf{v} - \boldsymbol{\rho}| = \sqrt{(x - x_v)^2 + (\zeta(x) - z_v)^2}. \tag{1}$$

Finally, the complex acoustic potential $p(\mathbf{M}_m, k, t)$ at the mth microphone and at wavenumber k is calculated as

$$p(\mathbf{M}_m, k, t) = p_0(k) P(\mathbf{M}_m, k) \exp(-\mathrm{i}kct), \tag{2}$$

where $p_0(k)$ is the amplitude of the emitted signal, or its complex Fourier coefficient at wavenumber k, and

$$P(\mathbf{M}_m, k) = \frac{\mathrm{e}^{-\mathrm{i}\pi/4}}{\sqrt{k8\pi}} \int \frac{D(\theta(\boldsymbol{\rho} - \mathbf{S})) \exp\{\mathrm{i}k[R(\mathbf{M}_m, \boldsymbol{\rho}) + R(\mathbf{S}, \boldsymbol{\rho})]\}}{\sqrt{R(\mathbf{S}, \boldsymbol{\rho}) R(\mathbf{M}_m, \boldsymbol{\rho})} \sqrt{[R(\mathbf{S}, \boldsymbol{\rho}) + R(\mathbf{M}_m, \boldsymbol{\rho})]}} \left\{ \left[1 + \frac{\mathrm{i}}{kR(\mathbf{S}, \boldsymbol{\rho})} \right] \left[\frac{(x - x_s)}{R(\mathbf{S}, \boldsymbol{\rho})} \frac{\mathrm{d}\zeta}{\mathrm{d}x} - \frac{(\zeta - z_s)}{R(\mathbf{S}, \boldsymbol{\rho})} \right] \right.$$
$$\left. + \left[1 + \frac{\mathrm{i}}{kR(\mathbf{M}_m, \boldsymbol{\rho})} \right] \left[\frac{(x - x_m)}{R(\mathbf{M}_m, \boldsymbol{\rho})} \frac{\mathrm{d}\zeta}{\mathrm{d}x} - \frac{(\zeta - z_m)}{R(\mathbf{M}_m, \boldsymbol{\rho})} \right] \right\} \mathrm{d}x. \tag{3}$$

Hereafter only the non-dimensional time-independent factor $P(\mathbf{M}_m, k)$ is considered, without loss of generality.

Eq. (3) describes the relation between the acoustic field at one location $\mathbf{M}_m$ and the shape of the rough surface. If ζ is assigned at a discrete set of locations x_r, the equation can be evaluated numerically using a quadrature method. Such an approach has been validated numerically and experimentally in the past, for static [37] and slowly moving [17,42,43] surfaces. Its accuracy was found comparable to that of a standard boundary element method for surfaces with similar characteristics to the ones considered here [43], which satisfied the Kirchhoff approximation condition. The solution of the inverse problem, i.e., the estimation of $\zeta(x_r)$ knowing $P(\mathbf{M}_m, k)$, is difficult because of the strongly nonlinear character of Eq. (3). A simplified approach proposed by Krynkin et al. [17] and common to all the techniques discussed here consists in isolating (within the integral) the terms of Eq. (3) that depend on ζ from the ones that depend on $\mathbf{M}_m$. In this way, the numerical solution of the forward problem takes the form of a matrix product,

$$\mathbf{F}^{(k)}_{N_m\times 1} = \mathbf{H}^{(k)}_{N_m\times N_r}\mathbf{E}^{(k)}_{N_r\times 1}, \tag{4}$$

where $\mathrm{H}^{(k)}_{m,r} = H(x_r, \mathbf{M}_m, k)$ is the element of a transfer matrix from a point x_r on the surface to a microphone in $\mathbf{M}_m$, $\mathrm{F}^{(k)}_m = F(P(\mathbf{M}_m, k))$ is a function of the acoustic potential at the mth microphone, and $\mathrm{E}^{(k)}_r = E(\zeta(x_r), k)$ is a function of the surface elevation at the location x_r. N_m and N_r are the number of microphones and the number of grid points that discretize the surface, respectively.

Eq. (4) can be inverted easily if the number of microphones equals the number of points where the surface is reconstructed, but this is seldom achievable given that the discretization grid must be fine enough for the numerical integration to converge. A solution [17], is to apply a singular value decomposition (SVD) [44] along with a regularization procedure to approximate an inverse of matrix $\mathbf{H}$. Following [17], here the regularization was performed in the sense of Tikhonov, and the regularization parameter was selected by the generalized cross-validation (GCV) method [45]. Then, vector $\mathbf{E}$ can be calculated from the known $\mathbf{F}$, and the surface elevation can be calculated independently at each point of the grid by inverting the function E as $\zeta(x_r) = E^{-1}(\zeta(x_r), k)$. The way to obtain a formulation similar to that of Eq. (4) starting from Eq. (3) differs for the three main approaches considered here, although it can be summarized into two main steps: a first expansion step common to all methods, and a subsequent separation of variables.

2.1. Expansion step: all methods

To simplify the dependence of P on ζ, the following assumptions must be introduced into Eq. (3): (i) the maximum surface elevation is small compared to the distance of the source and microphones from the surface, $\zeta/R \ll 1$; (ii) the source and the microphones are in the far-field of the surface, $kR \gg 1$; (iii) the surface gradient is small, $\mathrm{d}\zeta/\mathrm{d}x \ll 1$. As a result,

$$P(\mathbf{M}_m, k) \approx \int \mathcal{A}(\mathbf{S}, \mathbf{M}_m, x, k)\exp\left[-\mathrm{i}q_z(\mathbf{M}_m, \mathbf{S}, x, k)\zeta(x)\right]\mathrm{d}x, \tag{5}$$

where

$$q_z(\mathbf{M}_m, \mathbf{S}, x, k) = k\left[\frac{z_m}{R(\mathbf{M}_m, \boldsymbol{\rho}_0)} + \frac{z_s}{R(\mathbf{S}, \boldsymbol{\rho}_0)}\right], \tag{6}$$

$\boldsymbol{\rho}_0$ is the projection of $\boldsymbol{\rho}$ onto the x-axis, $\boldsymbol{\rho}_0 = (x, 0)$, and

$$\mathcal{A}(\mathbf{S}, \mathbf{M}_m, x, k) = \frac{\mathrm{e}^{-\mathrm{i}\pi/4}}{k\sqrt{k8\pi}}\frac{D(\theta(\boldsymbol{\rho}_0 - \mathbf{S}))\exp\{\mathrm{i}k[R(\mathbf{M}_m, \boldsymbol{\rho}_0) + R(\mathbf{S}, \boldsymbol{\rho}_0)]\}}{\sqrt{R(\mathbf{S}, \boldsymbol{\rho}_0)R(\mathbf{M}_m, \boldsymbol{\rho}_0)}\sqrt{[R(\mathbf{S}, \boldsymbol{\rho}_0) + R(\mathbf{M}_m, \boldsymbol{\rho}_0)]}}q_z(\mathbf{M}_m, \mathbf{S}, x, k). \tag{7}$$

In Eq. (5), the surface shape appears only inside the exponential. However, q_z still varies with $\mathbf{M}_m$. In [8], this dependence was removed by arranging the sensors along a curve where q_z is constant. In this way, the factors depending on ζ could be separated within the integral. The same result is accomplished by the three methods discussed here by means of an average or expansion. The consequent definition of the three matrices $\mathbf{F}$, $\mathbf{H}$, and $\mathbf{E}$, differentiates the three methods, as outlined below.

2.2. Separation of variables: SA method

This is the method presented by Krynkin et al. [17]. Here, the way to remove the dependence of q_z from $\mathbf{M}_m$, hence to isolate ζ, is to approximate q_z with the function

$$\tilde{q}_z(\mathbf{S}, x, k) = q_z(\mathbf{M}_m, \mathbf{S}, x, k) + k\left[\frac{\tilde{z}_m}{R(\tilde{\mathbf{M}}, \boldsymbol{\rho}_0)} - \frac{z_m}{R(\mathbf{M}_m, \boldsymbol{\rho}_0)}\right] = k\left[\frac{\tilde{z}_m}{R(\tilde{\mathbf{M}}, \boldsymbol{\rho}_0)} + \frac{z_s}{R(\mathbf{S}, \boldsymbol{\rho}_0)}\right] \tag{8}$$

where $\tilde{\mathbf{M}} = (\tilde{x}_m, \tilde{z}_m)$ is a representative microphone location, for example the center of the array $\tilde{\mathbf{M}} = \sum_m \mathbf{M}_m/N_m$. The approximation of q_z is more accurate if $\mathbf{M}_m - \tilde{\mathbf{M}}$ is small, i.e., for a short array. Therefore, here the method is referred to as the Short Array (SA) method, although it remains accurate even for relatively long arrays, as demonstrated for example by Krynkin et al. [37].

With the SA method, the elements of the three matrices are defined as

$$\mathrm{F}_m^{(k)} = P(\mathbf{M}_m, k), \tag{9}$$

$$\mathrm{H}_{m,r}^{(k)} = \mathcal{A}(\mathbf{S}, \mathbf{M}_m, x_r, k)\Delta x, \tag{10}$$

where Δx is the x_r grid size, and

$$\mathrm{E}_r^{(k)} = \exp\{-\mathrm{i}\tilde{q}_z(\mathbf{S}, x_r, k)\zeta(x_r)\}. \tag{11}$$

Once the vector $\mathbf{E}$ has been calculated from the inversion of Eq. (4), ζ is found as

$$\zeta(x_r) = \mathrm{i}\frac{\ln\left[\mathrm{E}_r^{(k)}\right]}{\tilde{q}_z(\mathbf{S}, x_r, k)}. \tag{12}$$

2.3. Separation of variables: SA0 method

Due to the ill-posedness of the inverse scattering problem, the solution of Eq. (4) usually requires some type of regularization. A common regularization strategy, implemented for example by Krynkin et al. [17], and also here, is the so-called Tikhonov regularization [46]. The regularized solution in the sense of Tikhonov minimizes a weighted sum of the squared residual and of the norm of the solution [46], which corresponds here to the sum $\|\mathbf{F} - \mathrm{H}\mathbf{E}\|^2 + \beta^2\|\mathbf{E}\|^2$, where β is a regularization parameter. Accordingly, the Tikhonov regularization constrains the norm $\|\mathbf{E}\|^2$. However, for the SA method, $\mathrm{E} = \exp(-\mathrm{i}\tilde{q}_z\zeta) \to 1$ when $\tilde{q}_z\zeta \to 0$, therefore the optimal solution in the sense of Tikhonov can be biased, especially when the surface deformation is small.

The SA0 method consists in a simple preconditioning of the SA method, introduced for this work with the aim of fixing such an inconsistency. Note that

$$P(\mathbf{M}_m, k) - P_0(\mathbf{M}_m, k) \approx \int \mathcal{A}(\mathbf{S}, \mathbf{M}_m, x, k)\{\exp[-\mathrm{i}q_z(\mathbf{M}_m, \mathbf{S}, x, k)\zeta(x)] - 1\}\mathrm{d}x, \tag{13}$$

where $P_0(\mathbf{M}_m, k)$ is the acoustic field reflected from a flat surface $\zeta \equiv 0$. Unlike Eq. (6), the term that multiplies the kernel $\mathcal{A}$ is small when $k\zeta$ is small. The pre-conditioned problem is consistent with the Tikhonov regularization. However, solving Eq. (13) requires either the measurement or the theoretical calculation of P_0. The latter is straightforward, for example by means of Eq. (4). The replacement of q_z with $\tilde{q}_z$ is still necessary with this method.

With the SA0 method, the elements of the three matrices are defined as

$$\mathrm{F}_m^{(k)} = P(\mathbf{M}_m, k) - P_0(\mathbf{M}_m, k), \tag{14}$$

$$\mathrm{H}_{m,r}^{(k)} = \mathcal{A}(\mathbf{S}, \mathbf{M}_m, x_r, k)\Delta x, \tag{15}$$

and

$$\mathrm{E}_r^{(k)} = \exp[-\mathrm{i}\tilde{q}_z(\mathbf{S}, x_r, k)\zeta(x_r)] - 1. \tag{16}$$

ζ is calculated as

$$\zeta(x_r) = \mathrm{i}\frac{\ln\left[\mathrm{E}_r^{(k)} + 1\right]}{\tilde{q}_z(\mathbf{S}, x_r, k)}. \tag{17}$$

2.4. Separation of variables: SP method

This last method is based on a Small Perturbation (SP) expansion [e.g., 41, ch. 3], which only applies to a small surface elevation $q_z\zeta \ll 1$. The derivation is similar to the ones described in [11] and [34] for an electromagnetic problem, but here the inversion is obtained without iterations and without resorting to Fourier analysis, for a potentially underdetermined system of equations. Expanding the exponential in Eq. (13) at first order yields

$$P(\mathbf{M}_m, k) - P_0(\mathbf{M}_m, k) \approx -\mathrm{i}\int \mathcal{A}(\mathbf{S}, \mathbf{M}_m, x, k)q_z(\mathbf{M}_m, \mathbf{S}, x, k)\zeta(x)\mathrm{d}x. \tag{18}$$

Then, ζ is already isolated and there is no need to approximate the function q_z. The elements of the three matrices are defined as

$$\mathrm{F}_m^{(k)} = P(\mathbf{M}_m, k) - P_0(\mathbf{M}_m, k), \tag{19}$$

$$\mathrm{H}_{m,r}^{(k)} = -\mathrm{i}q_z(\mathbf{M}_m, \mathbf{S}, x, k)\mathcal{A}(\mathbf{S}, \mathbf{M}_m, x_r, k)\Delta x, \tag{20}$$

and

$$\mathrm{E}_r^{(k)} = \zeta(x_r). \tag{21}$$

ζ is obtained directly from the inversion as $\zeta(x_r) = \mathrm{E}_r^{(k)}$.

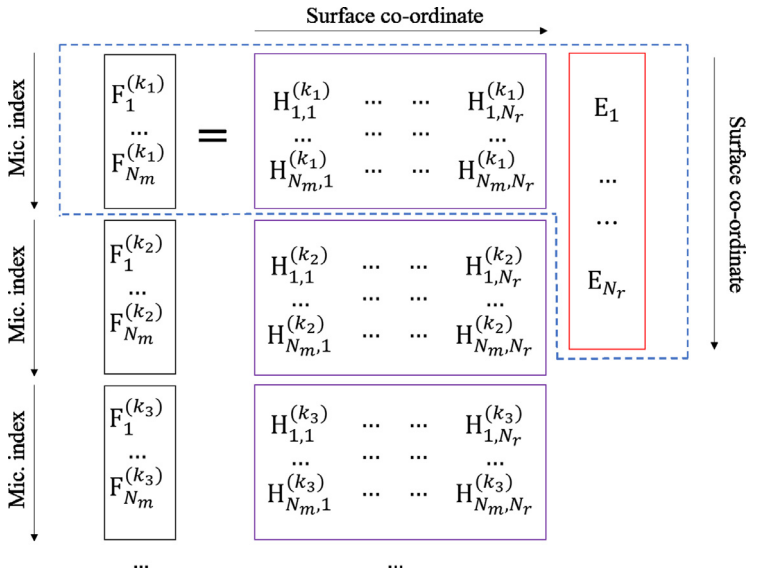

Fig. 2. Schematic representation of the linearized forward problem cast as matrix product. The single-frequency (standard) approach is represented by the terms inside the dashed line: the unknown surface shape is represented by the vector $\mathbf{E}_{N_r\times 1}$, and is obtained from the complex pressure $\mathrm{F}_{\mathrm{m}}^{(k_1)}$ measured at each microphone $m = 1 \dots N_m$, by inverting the rectangular known transfer matrix $\mathbf{H}_{N_m\times N_r}^{(k_1)}$ numerically. The multiple frequency approach is obtained by concatenating matrices $\mathbf{F}_{N_m\times 1}^{(k_j)}$ and $\mathbf{H}_{N_m\times N_r}^{(k_j)}$ obtained for different wavenumbers k_j, $j = 1, \dots, N_k$, while $\mathbf{E}_{N_r\times 1}$ remains unchanged.

2.5. Multiple frequency extension

All three approaches described above typically require a numerical inversion scheme to solve a sometimes largely underdetermined linear system. As it will be shown, the accuracy of the reconstruction depends strongly on the numerical inversion, and on the presence of noise. Furthermore, the choice of the signal frequency affects the results in such a way that it is difficult to identify an optimal frequency without knowledge of the surface statistics. To overcome these issues, here it is suggested to extend the three methods above, combining information available at different frequencies in order to improve the robustness of the surface reconstruction.

It is assumed that the same surface can be tested at multiple wavenumbers k_j, $j = 1, \dots, N_k$, either using harmonic signals at subsequent times, or simultaneously with a sine sweep or a random noise. For each frequency, an equation like Eq. (4) applies. For the SP method, the unknown vector $\mathrm{E}_{N_r\times 1}$ is independent from k, while for the SA and SA0 methods it is a function of the frequency through $\tilde{q}_z$. For these methods, $\tilde{q}_z$ can be approximated by its average across multiple frequencies, $\tilde{q}_k$. Since $\tilde{q}_z$ is directly proportional to k, the error introduced with such approximation is proportional to the bandwidth. Then,

$$\mathrm{E}_r^{(k)} \approx \mathrm{E}_r = \begin{cases} \exp\left[-\mathrm{i}\tilde{q}_k(\mathbf{S}, x_r)\zeta(x_r)\right], & \text{SA method,} \\ \exp\left[-\mathrm{i}\tilde{q}_k(\mathbf{S}, x_r)\zeta(x_r)\right] - 1, & \text{SA0 method,} \\ \zeta(x_r), & \text{SP method.} \end{cases} \tag{22}$$

Finally, a larger multi-frequency system can be constructed by using vertical concatenation (Fig. 2), as

$$\begin{bmatrix} \mathbf{F}_{N_m\times 1}^{(k_1)} \\ \vdots \\ \mathbf{F}_{N_m\times 1}^{(k_{N_k})} \end{bmatrix} = \begin{bmatrix} \mathbf{H}_{N_m\times N_r}^{(k_1)} \\ \vdots \\ \mathbf{H}_{N_m\times N_r}^{(k_{N_k})} \end{bmatrix} \mathbf{E}_{N_r\times 1}, \tag{23}$$

and ζ can be estimated from $N_m N_k$ data obtained at N_m microphones, by inverting a much larger matrix with size $N_m N_k \times N_r$. When $N_m N_k > N_r$, the system becomes overdetermined, and the solution can be found for example with a least squares method. As it will be seen in Section 4, this can strongly improve the robustness of the inversion.

3. Numerical study of the inversion uncertainty

3.1. Numerical model

The performance of the various reconstruction methods presented in the previous section is here investigated numerically with a Monte Carlo approach. The scripts used for the numerical simulations and analysis can be found in [47]. The acoustic

field is calculated numerically by means of Eq. (3) for a large number of realizations of the surface function ζ, generated by means of a linear random phase model. The acoustic model has been previously validated for similar surfaces by Dolcetti and Krynkin [42] in forward scattering, and by Dolcetti et al. [43] in a backscattering configuration. A further test of convergence with respect to the density and extent of the surface discretization grid used for the numerical integration of Eq. (3) has been performed for this work, in the most stringent conditions (highest frequency, largest distance of the array from the surface). As a result, a grid spacing of 1 mm ($\Delta x/\lambda < 0.1$) with 2048 points is chosen to calculate Eq. (3) numerically. Further refinements or extensions of the grid caused variations of the magnitude and phase of the potential <1%. The synthetic acoustic field was then analyzed with the procedures described previously, yielding an estimate of the surface shape. The statistics of the reconstruction error are inferred by comparing the known initial realizations with their reconstructions.

The geometry of the measurement setup and the characteristics of the surface are defined in such a way to allow their characterization by a small number of parameters. Therefore, in contrast with the works of Krynkin et al. [17,37], a line-array setup is used in this work, i.e., the source and each microphone are all at the same height z_0 above the plane $z = 0$. The spacing between microphones is constant, and defined by the parameter d_0. The source is modeled as a baffled piston, with radius a_0 and with directivity [48, p. 381]

$$D(\theta) = 2\frac{J_1(ka_0\sin(\theta))}{ka_0\sin(\theta)}, \tag{24}$$

where J_1 is the Bessel function of the first kind, and θ is the angle with respect to the source axis. The axis is inclined by an angle ϕ_0 with respect to the horizontal direction. The microphones are modeled as omnidirectional. To give a more realistic representation and take into account the physical dimensions of the source, a minimum fixed distance equivalent to 60 mm (2.6 to 4.4 times the acoustic wavelength) is imposed from the first microphone to the source in all simulations.

The rough surface realizations are constructed by means of a linear random phase model, in a way similar to Thorsos [40]:

$$\zeta_n(x_q) = \sum_{\nu}\sqrt{\frac{\Psi(\kappa_\nu)}{2}}\left[\xi_{\nu,n}\exp(\mathrm{i}\kappa_\nu x_q) + \xi^*_{\nu,n}\exp(-\mathrm{i}\kappa_\nu x_q)\right] \tag{25}$$

where the superscript $*$ indicates the complex conjugate, $\kappa_\nu = \nu 2\pi/L$, $\nu = 1,\ldots L/2\Delta x$, L is the surface length, Δx is the surface grid size, $\xi_{\nu,n}$ is a Gaussian-distributed complex variable, and $\Psi(\kappa)$ is the surface Fourier power spectrum. Note that the discretization grid employed for the calculation of the acoustic potential (forward problem), x_q, is different in general from the reconstruction grid x_r introduced in Section 2. A power-function spectrum $\Psi(\kappa) \propto \kappa^{-\alpha_0}$ is used. Such a spectrum is commonly used to describe natural surfaces such as water waves in the ocean [49] and in rivers [42], or sea [50] and river [51] bed shapes. Similarly to the work in [51], a saturation range is introduced at wavenumbers $< \kappa_0$, as well as a small scale cut-off at wavenumber κ_1, i.e., the spectrum is given the form

$$\Psi(\kappa) = \begin{cases} \sigma_0^2 C, & \text{where } \kappa < \kappa_0, \\ \sigma_0^2 C\left(\dfrac{\kappa}{\kappa_0}\right)^{-\alpha_0}, & \text{where } \kappa_0 \le \kappa \le \kappa_1 \\ 0, & \text{where } \kappa > \kappa_1, \end{cases} \tag{26}$$

where C is a normalization constant, σ_0 is the standard deviation of the surface elevation, $\kappa_0 = 2\pi/l_0$ is the lower saturation wavenumber, and $\kappa_1 = 2\pi/l_1$ is the upper cut-off wavenumber. The saturation scale κ_0 defines a maximum scale of the surface, and ensures that the statistical moments converge independently of the surface size.

Finally, the problem is entirely defined by 9 parameters. Four of them (σ_0, α_0, κ_0, and κ_1) define the statistics of the surface, two (z_0 and d_0) the geometry of the acoustic array, and three more (a_0, ϕ_0, and k_0) the characteristics of the source. The last parameter, $k_0 = 2\pi/\lambda_0$, is the wavenumber of the acoustic signal, or the average of all wavenumber components used for the analysis in the multiple-frequency calculations. All calculations in sections 3.2 to 3.7 are based on a signal with a single frequency. The effect of the multiple frequency extension is discussed in Section 3.8, and with the experimental results in Section 4.2.

3.2. Error metrics

For various combinations of the 9 parameters, the performance of the different reconstruction approaches is tested numerically on 1000 random realizations of the rough surface constructed by means of Eq. (25). $\tilde{\zeta}_n(x_r)$ is defined as the estimated reconstruction of the nth surface realization $\zeta_n(x_r)$. Then, the reconstruction error at each grid point x_r and realization is $\varepsilon_n(x_r) = \tilde{\zeta}_n(x_r) - \zeta_n(x_r)$. Binning the values of $\varepsilon_n(x_r)$ observed across all realizations yields a set of histograms that estimate the probability distribution function (pdf) of the error at each x_r.

Fig. 3 shows examples of these normalized histograms obtained for the SA and SA0 methods, for two sets of surfaces that differed only for their standard deviation of the surface function, $\sigma_0/\lambda_0 = 0.06$ and $\sigma_0/\lambda_0 = 0.12$, respectively. Although the error statistics are markedly different in the four cases shown in Fig. 3, five characteristic regions of the plots where the histograms behave similarly can be identified. These are designated with letters A, B, and C. The two areas indicated with C are at the edges of the reconstructed surface. Here, the error distribution is multi-modal, and the error is large,

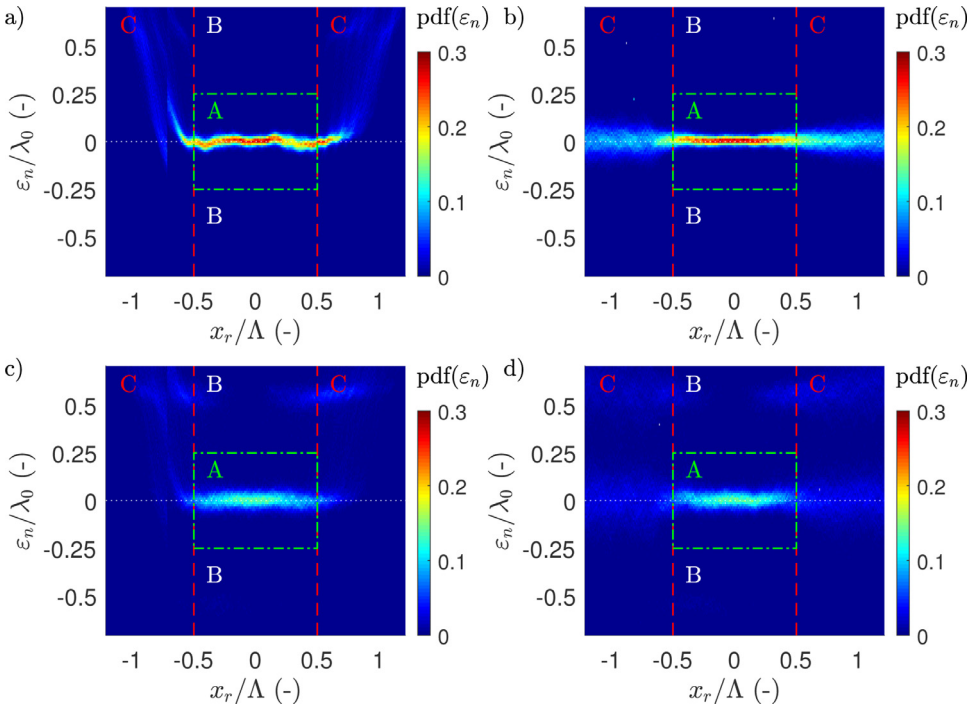

Fig. 3. Probability distribution of the local surface reconstruction error $\varepsilon_n = \tilde{\zeta}_n(x_r) - \zeta_n(x_r)$ evaluated from 1000 realizations. Geometry and surface parameters: $\alpha_0 = 4$, $\kappa_0/k_0 = 0.34$, $\kappa_1/k_0 = 3.4$, $z_0/\lambda_0 = 18$, $d_0/\lambda_0 = 0.59$, $k_0 a_0 = 7.4$, $\psi_0 = \pi/3$ rad, $N_m = 34$ microphones. (a, b) $\sigma_0/\lambda_0 = 0.059$, (c, d) $\sigma_0/\lambda_0 = 0.118$. (a, c) SA method, (b, d) SA0 method. The vertical dashed lines indicate the boundaries of the effective reconstruction domain, comprised between the specular reflection points for the first and last microphone. The rectangular region A with green contours identifies the domain used for the computation of the error metrics. (For interpretation of the references to colour in this figure legend, the reader is referred to the web version of this article.)

especially for the SA method. The distance between the peaks of the distribution is approximately $\lambda_0/2$. Since both the SA and SA0 methods obtain the surface from the phase of a term proportional to $\exp(-\mathrm{i}\tilde{q}_z\zeta)$, the multiple modes may have occurred due to an ambiguity of the phase. The boundaries between the outer C regions and the inner A and B region in Fig. 3 are represented by the points of specular reflection of the first and last microphones of the array, $(x_s + x_{m,1})/2$ and $(x_s + x_{m,N_m})/2$, respectively. The portion of the surface in between these points, with size $\Lambda = (x_{m,N_m} - x_{m,1})/2$, was identified as the effective domain of the reconstruction [17]. Here, in this region, the error distribution appears narrower and with a clearer peak centered near $\varepsilon_n = 0$, except for the SA method at smaller σ_0, which shows a visible fluctuation of the peak location along the surface. A broader distribution indicates a larger deviation between target and reconstructed surface, while the distance of the peak from zero indicates a bias of the reconstruction. Secondary peaks of the distributions are visible in region B. Such large errors here indicate a failure of the reconstruction for some realizations, which could strongly skew the statistical moments. In this work, a reconstruction is considered to have failed when the maximum of the error (within the reconstruction domain Λ) falls in region B, i.e., when $\max|\varepsilon_n(x_r)| > \lambda_0/4$.

To give a simple quantitative representation of the reconstruction error that takes into account the complexity of the observed distributions, three error metrics are defined. The error in the regions C is not considered for the calculation of these metrics. The likelihood of a failure of the reconstruction is estimated with the parameter F_ε, defined as the ratio between the number of failed reconstructions and the total number of realizations, N,

$$F_\varepsilon = \frac{1}{N}\sum_n b(n), \quad b(n) = \begin{cases} 1 & \max|\varepsilon_n(x_r)| > \lambda_0/4, x_r \in \Lambda, \\ 0 & \text{otherwise.} \end{cases} \tag{27}$$

This metric is assumed to represent the robustness of an algorithm. The remaining two metrics are defined considering only the realizations that do not fall into the failure criterion (i.e., with reference to region A in Fig. 3). They represent the uncertainty (bias and deviation) that can be expected from a reconstruction that does not appear obviously wrong. Excluding the realizations that cross regions B, the 15.87%, 50%, and 84.14% percentiles of the $\varepsilon_n(x_r)$ distribution are calculated at each location x_r within the reconstruction domain Λ. The bias P_ε is defined as the root-mean-square (rms) average of the 50% percentile (median) error level calculated over x_r. The reconstruction deviation, S_ε, is instead defined as the rms average of the difference between the 84.14% and 15.87% error levels, corresponding to a 68.27% confidence interval. To quantify the uncertainty of the error metrics computed by the Monte Carlo simulation, these were calculated for five independent sets of

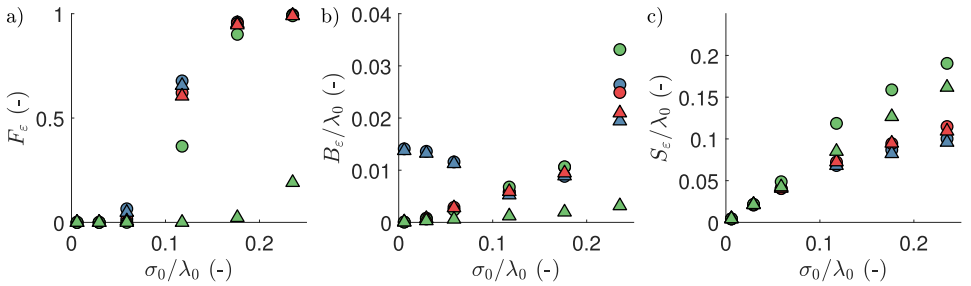

Fig. 4. Effect of the model approximations and numerical inversion procedure on the error metrics, for the three inversion methods: SA (blue), SA0 (red), and SP (green). The circles represent calculations with the standard procedure, applying the inversion to the synthetic pressure distribution determined by a Kirchhoff approximation, Eq. (3). The triangles represent the error attributable to the numerical inversion only. Results shown for $\alpha_0 = 4$, $\kappa_0/k_0 = 0.34$, $\kappa_1/k_0 = 3.4$, $k_0 a_0 = 7.4$, $\psi_0 = \pi/3$ rad, $N_m = 34$, $z_0/\lambda_0 = 18$. (For interpretation of the references to colour in this figure legend, the reader is referred to the web version of this article.)

1000 surfaces each, with similar statistics, using the same setup and surface parameters of Fig. 3a. The maximum variations of the metrics across the five sets was found to be ±3% for F_ε, ±2.5% for B_ε, and ±0.5% for S_ε.

Note that during the formalization of the inversion problem, the location of the points where the surface shape is calculated, x_r, is arbitrary. Here, x_r is represented by a regular grid with length L_0 and spacing Δx_r. It should be noted that, although the reconstruction is accurate only within a limited portion of the reconstruction grid, bounded by the first and last stationary phase points, setting $L_0 = \Lambda$ does not provide accurate reconstructions. The errors were found to decrease with an increase of L_0, until $L_0 > 5\Lambda$. Further increases of L_0 have a non-significant effect on the error metrics. Hence, all calculations reported here were conducted using $L_0 = 6\Lambda = 3(x_{m,N_m} - x_{m,1})$. The simulations were found being marginally affected by the reconstruction grid size Δx, as long as this was small enough to be able to resolve the smallest surface scales. A variation of the three metrics smaller than 1.1% was observed for Δx between $0.025\lambda_0$ and $0.4\lambda_0$. A value of $\Delta x < 0.1\lambda_0$ has been used for all simulations.

3.3. Self consistency

The reconstruction algorithms examined here rely on three approximations: (i) a far-field expansion of the Kirchhoff integral formula; (ii) a discretization and truncation of the scattering surface; (iii) a separation of variables leading to a linearization of the problem, obtained either by expanding q_z at a single location (SA, SA0), or by taking the small perturbation limit $q_z\zeta \ll 1$ (SP). Each of these approximations is likely to introduce an error in addition to the one that arises from the numerical inversion. To examine the impact of these additional error sources, the reconstruction was applied to an 'ideal' scenario, where the above approximations should not contribute. In this scenario, the acoustic pressure was estimated using Eq. (4), which already includes all the above approximations, instead of Eq. (3). In this way, any error observed after the inversion would be a result of the numerical inversion procedure alone.

Fig. 4 shows a comparison of the error metrics calculated with the standard procedure (synthetic pressure signal estimated from Eq. (3)), and based on the ideal scenario (Eq. (4)), for the three methods and for a range of surface standard deviations, σ_0/λ_0 between 0.006 and 0.24. The probability of failure F_ε was found to increase sharply with σ_0/λ_0 when $\sigma_0\lambda_0 \geq 0.1$, for all methods. B_ε also increased with σ_0 for the SA0 and SP methods. The SA method showed a considerable bias also for small σ_0, and displayed a minimum of B_ε at $\sigma_0/\lambda_0 \approx 0.1$. Moreover, the deviation S_ε increased with σ_0 for all methods, with larger values observed for SP at large σ_0/λ_0 when the $q_z\zeta \ll 1$ approximation ceased to be valid.

For the SA and SA0 methods, the difference between the more realistic case and the ideal case was generally not significant, indicating that the reconstruction error was dominated by the numerical inversion procedure. Visible differences observed at $\sigma_0/\lambda_0 = 0.24$ may have been caused by the very small number of successful reconstructions for this case ($F_\varepsilon \approx 1$) which strongly reduced the number of successful realizations used for the calculation of B_ε and S_ε. The SP-based reconstruction showed a significant decrease of all error metrics when the expansion errors were removed, especially when $\sigma_0/\lambda_0 > 0.1$. This was to be expected, since the SP model looses validity when $\sigma_0/\lambda_0 \sim 1$. These calculations confirm that the approximations introduced by Krynkin et al. [17] to transform the integral Kirchhoff equation into an invertible linear system of equations are appropriate, at least for the cases considered here. Note that, during a similar self-consistency test, Wombell and DeSanto [8] observed a much larger difference between the 'realistic' and 'ideal' case reconstruction at large σ_0/λ_0. However, the difference between the two cases in [8] was determined by the applicability of the Kirchhoff approximation, which has been assumed valid in both cases here. The difference observed here, instead, was due only to the expansion and factorization steps.

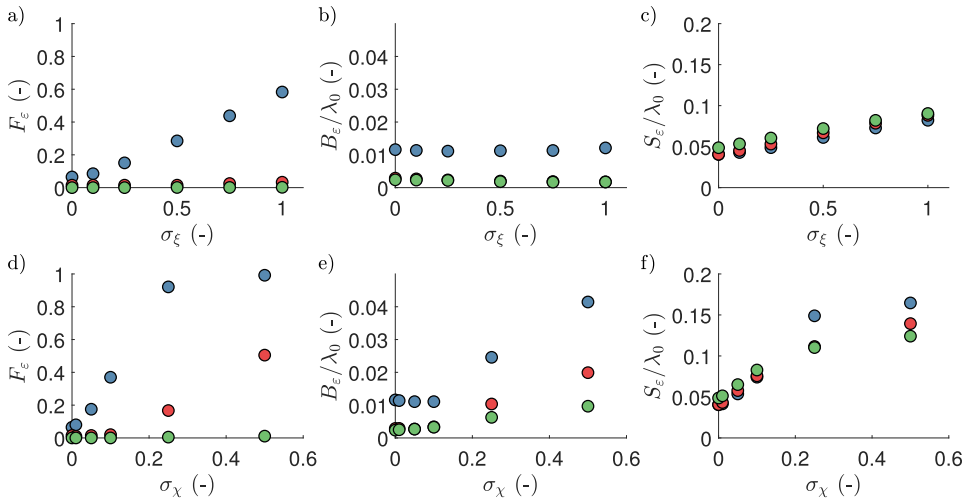

Fig. 5. Effect of Gaussian amplitude uncertainty, σ_ξ (a, b, c), and phase uncertainty, σ_χ (d, e, f), on the error metrics, for the three inversion methods: SA (blue), SA0 (red), and SP (green). Results shown for $\sigma_0/\lambda_0 = 0.06$, $\alpha_0 = 4$, $\kappa_0/k = 0.34$, $\kappa_1/k = 3.4$, $k_0 a_0 = 7.4$, $\psi_0 = \pi/3$ rad, $N_m = 34$, $z_0/\lambda_0 = 18$. (For interpretation of the references to colour in this figure legend, the reader is referred to the web version of this article.)

3.4. Effects of measurement noise

The robustness of each method to noise was assessed by introducing additive Gaussian noise to either the amplitude or phase of the synthetic signal, i.e.,

$$P_\nu(\mathbf{M}_m, k) = P(\mathbf{M}_m, k)(1 + \xi)\exp(\mathrm{i}\chi 2\pi), \tag{28}$$

where P_ν is the 'noisy' signal, and ξ and χ are Gaussian distributed random variables. Their respective standard deviations, σ_ξ and σ_χ, represent the magnitude of the amplitude and phase noise, respectively. Examples of the error metrics calculated for different values of σ_ξ and σ_χ (keeping $\sigma_\chi = 0$ or $\sigma_\xi = 0$, respectively) are shown in Fig. 5. Amplitude noise increased the probability of failure F_ε only for SA, but increased the deviation S_ε similarly for all methods. The bias B_ε was not affected. Phase noise had a stronger effect on all metrics, and for all methods, except the probability of failure of SP which remained very low even with large σ_χ. The strongest effect was observed for the SA method, where a phase uncertainty of 20% was found sufficient to bring the probability of failure above 0.9. Random variations of the phase similar to those modeled with σ_χ can be caused by uncertainties of the microphone locations, or lack of phase calibration. The rapid increase of S_ε (and of F_ε for SA) with σ_χ can severely harm the overall accuracy of the method, and requires care while setting up the measurement system.

3.5. Effects of the measurement setup

The measurement setup is defined by the parameters z_0, d_0, a_0, and ϕ_0. Variations of the speaker radius a_0 and angle ϕ_0 mainly affect the distribution of the incident sound intensity on the surface, and were found having small effect on the error metrics as long as the insonified area was larger than the whole reconstruction domain. For all simulations considered here, the product $k_0 a_0 = 7.4$ was held constant and ϕ_0 was fixed at 60 degrees from the horizontal. While evaluating the effects of the height z_0 and microphone separation d_0 on the reconstruction errors, the position of the first and last specular points were held constant to keep the reconstruction domain identical. For a given number of microphones N_m, the locations of the first and last microphones were determined as $x_{m,1} = 2x_{sp,1} - x_s$ and $x_{m,N_m} = 2x_{sp,N_m} - x_s$, respectively, where $x_{sp,1}$ and x_{sp,N_m} define the position of the two specular points. Then, d_0 followed from $d_0 = (x_{m,N_m} - x_{m,1})/(N_m - 1)$.

The values of the three error metrics, calculated for different combinations of z_0/λ_0 between 8.8 and 29.4, and for d_0/λ_0 between 0.37 and 2.7, are shown in Figs. 6–8, respectively. Each row in these figures was calculated with a different frequency, to test the non-dimensionalization of the error metrics and parameters by the acoustic wavelength. The axis ranges differ between rows due to the non-dimensionalization. For all methods, the probability of failure (Fig. 6) increased sharply when $d_0/\lambda_0 \leq 0.5$. For larger microphone separations, the SA0 and SP methods showed a small $F_\varepsilon < 5\%$. In contrast, the SA method showed a further increase of F_ε when $d_0/\lambda_0 > 1.5$, with estimated probability of failure well above 50%. This indicates a lack of robustness of the SA method.

The SA method performed poorly also with respect to the error bias, as shown in Fig. 7. Here, the relative bias B_ε/λ_0 was of the order of 1% for the SA method, almost one order of magnitude larger than for SA0 and SP. A different color scale was used for the SA plots in Fig. 7, to account for this difference. For these simulations, σ_0/λ_0 was between 4.4% and 7.4%, therefore the bias was a significant proportion of the standard deviation of the surface roughness. The smallest

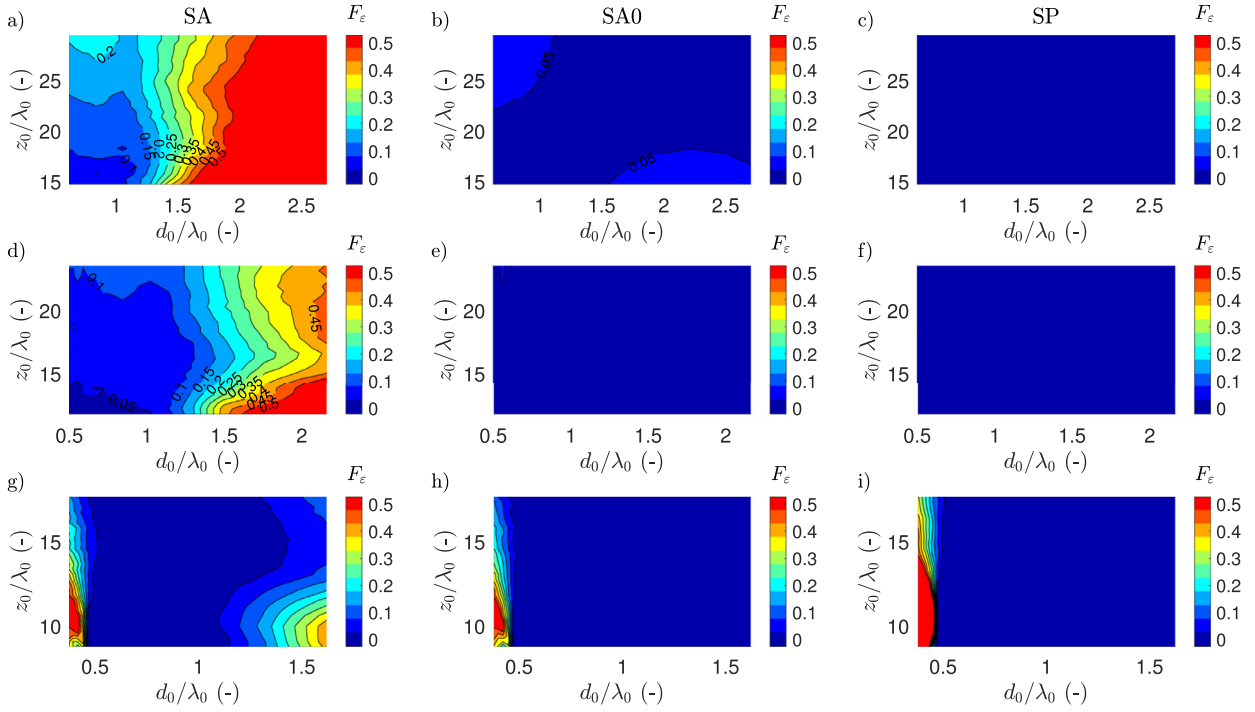

Fig. 6. Distribution of the probability of failure F_ε as a function of the array height z_0 and microphone spacing d_0, for the three methods: SA (a, d, g), SA0 (b, e, h), and SP (c, f, i). Geometry and surface parameters: $\alpha_0 = 4$, $k_0 a_0 = 7.4$, $\psi_0 = \pi/3$ rad. (a, b, c) $\sigma_0/\lambda_0 = 0.074$, $\kappa_0/k_0 = 0.27$, $\kappa_1/k_0 = 2.7$, $f_0 = 25$ kHz, (d, e, f) $\sigma_0/\lambda_0 = 0.059$, $\kappa_0/k_0 = 0.34$, $\kappa_1/k_0 = 3.4$, $f_0 = 20$ kHz, (g, h, i) $\sigma_0/\lambda_0 = 0.044$, $\kappa_0/k_0 = 0.45$, $\kappa_1/k_0 = 4.5$, $f_0 = 15$ kHz. The simulations were performed with the same dimensional parameters, for different excitation frequencies. The non-dimensional axis ranges are different for each row as a result.

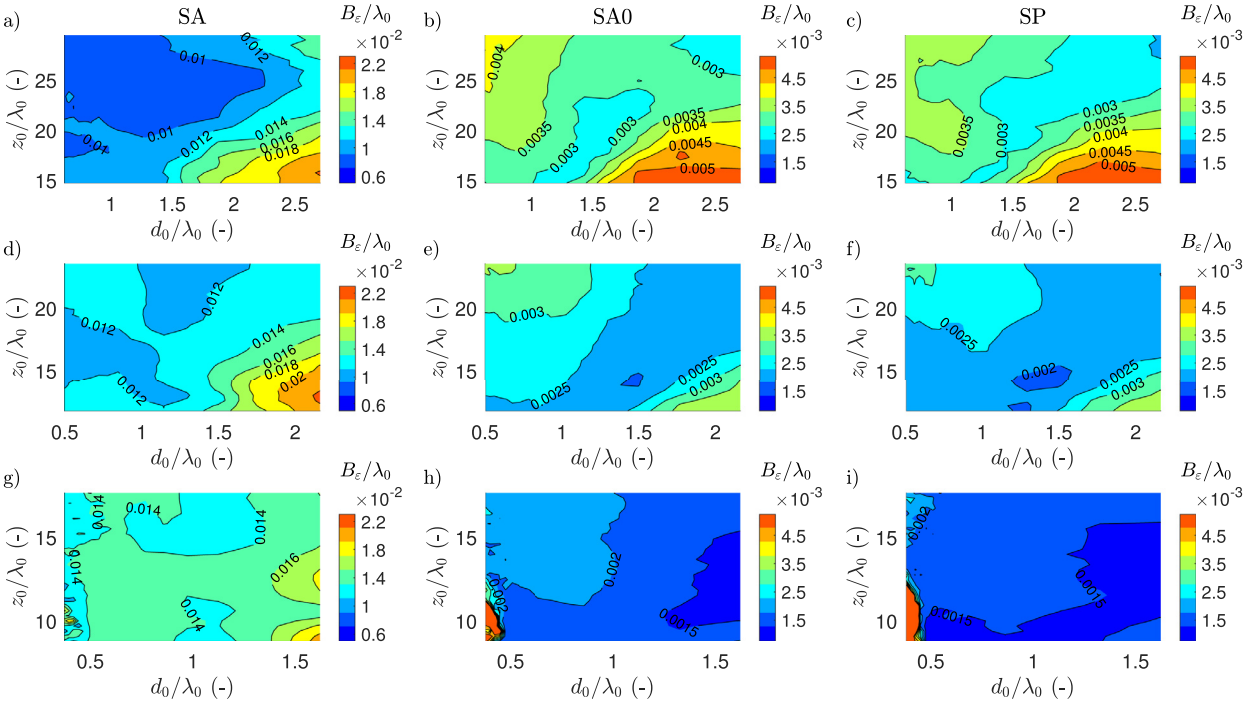

Fig. 7. Distribution of the non-dimensional error bias B_ε/λ_0 as a function of the array height z_0 and microphone spacing d_0, for the three methods: SA (a, d, g), SA0 (b, e, h), and SP (c, f, i). Geometry and surface parameters are the same as in Fig. 6. Note the different color-coding in (a), (d), and (g).

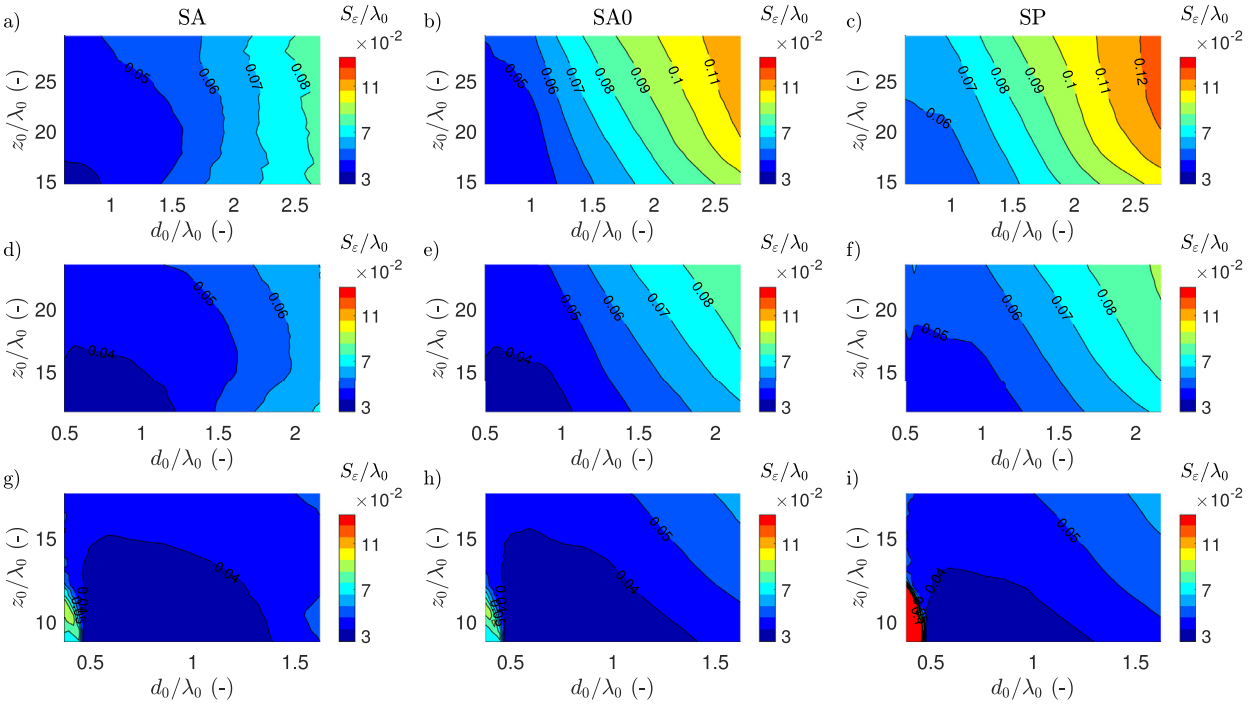

Fig. 8. Distribution of the non-dimensional reconstruction uncertainty S_ε/λ_0 as a function of the array height z_0 and microphone spacing d_0, for the three methods: SA (a, d, g), SA0 (b, e, h), and SP (c, f, i). Geometry and surface parameters are the same as in Fig. 6.

bias seemed to occur at larger σ_0/λ_0 for the SA method, in accordance with what has been observed in Fig. 3. In contrast, the SA0 and SP methods had smaller bias at smaller σ_0/λ_0. For all methods, an increase of B_ε/λ_0 at large microphone separation $d_0/\lambda_0 > 2$ and small height $z_0/\lambda_0 < 20$ was observed. To maintain the bias small, an increase of the separation between the microphones must be accompanied by an increase of the height of the array above the surface. The behavior of the deviation S_ε, in contrast, was similar for the three algorithms, as shown in Fig. 8. S_ε was generally larger when the microphones separation d_0/λ_0 and array height z_0/λ_0 were large. Therefore, to minimize S_ε the array needs to be kept near the surface, and the distance between the microphones needs to be small (but larger than $0.5\lambda_0$). The observed values of S_ε/λ_0 were typically between 3% and 10%, which suggests that S_ε was the main contribution to the overall reconstruction error, at least for the SA0 and SP method.

3.6. Effects of the roughness parameters

The performance of the three reconstruction algorithms with respect to changes of the surface standard deviation σ_0 is investigated in Fig. 9a–c. The error metrics were calculated for various combinations of σ_0 (between 0.1 mm and 4 mm) and of the frequency f_0 (between 15 kHz and 25 kHz). The results are found reasonably consistent after normalization of σ_0, B_ε, and S_ε by the acoustic wavelength λ_0, although low-frequency data (triangles in Fig. 9a–c) had slightly larger values of the normalized error metrics. This might have been an effect of the difference of κ_0/k_0 and z_0/λ_0.

Although the reconstruction error appears to scale with the acoustic wavelength, the performance of the reconstruction is generally better described by the quantity S_ε/σ_0. This is apparent from Fig. 9c, where $S_\varepsilon/\sigma_0 = 1$ is represented with a dashed line. In fact, at low frequency (low σ_0/λ_0), although S_ε/λ_0 was very small for all methods, S_ε was very close to σ_0. This indicates an error as large as the amplitude of the surface roughness, which is generally not acceptable. The more meaningful error S_ε/σ_0 is indicated by the distance of all points from the line $S_\varepsilon/\sigma_0 = 1$. This distance increased for the SA and SA0 methods at higher frequencies ($\sigma_0/\lambda_0 > 0.1$), where S_ε/λ_0 became significantly lower than σ_0/λ_0, while it remained very small for the SP method due to the non applicability of the small perturbation expansion at high frequency.

The sensitivity of the error metrics to the surface spectrum slope α_0 is represented in Fig. 9d–f. A steeper spectrum (larger α_0) yields a smoother surface. This was associated with a slight decrease of F_ε and B_ε, and a more marked decrease of S_ε. Similarly, a smaller value of the characteristic roughness wavenumber κ_0 is associated with a gentler surface. These also corresponded to smaller B_ε and S_ε, for all algorithms (Fig. 9h-i). F_ε, however, showed a maximum at $\kappa_0/k_0 \approx 0.5$ (Fig. 9g), which is currently difficult to motivate physically. The shorter cut-off scale represented by κ_1 was found having no significant impact on the error metrics, at least in the range $1.1 \leq \kappa_1/k_0 \leq 8.5$ (plot omitted). This suggests that the inversion acts as an effective low-pass filter of the roughness function.

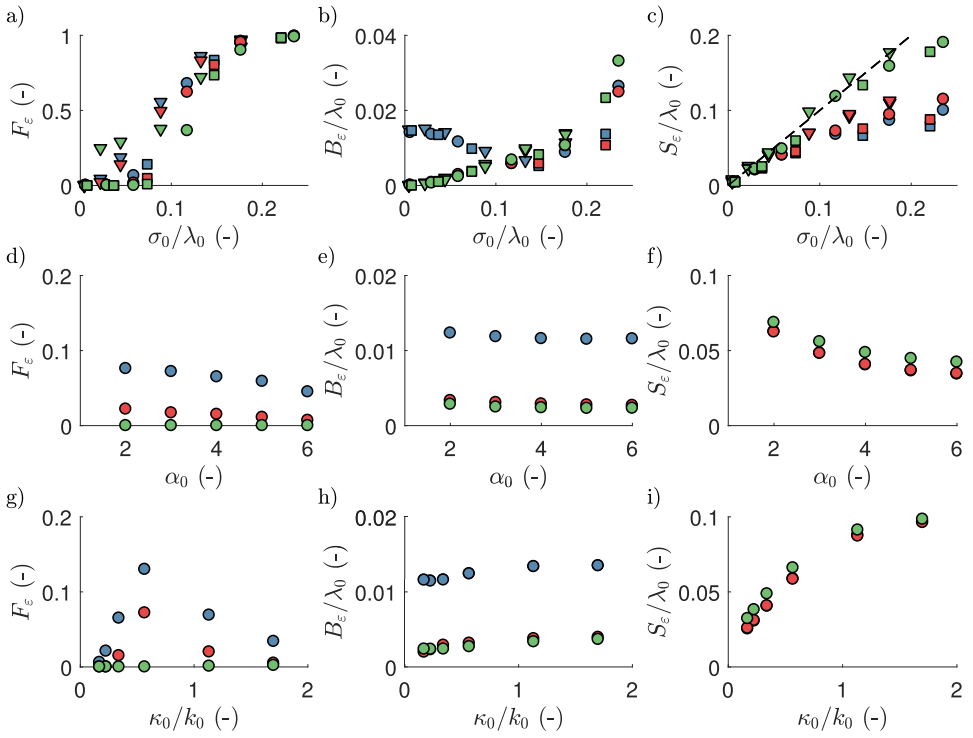

Fig. 9. Effect of surface roughness standard deviation (a, b, c), spectrum slope (d, e, f), and characteristic surface wavenumber (g, h, i) on the error metrics, for the three inversion methods. SA (blue), SA0 (red), and SP (green). The different symbols in (a, b, c) denote different frequencies: 15 kHz (triangles), 20 kHz (circles), 25 kHz (squares). The dashed line in (c) indicates $S_\varepsilon = \sigma_0$. Geometry and surface parameters: (a, b, c), $\kappa_0/k_0 = 0.45$, $z_0/\lambda_0 = 13$ (triangles), $\kappa_0/k_0 = 0.27$, $z_0/\lambda_0 = 22$ (squares); for all remaining, $\sigma_0/\lambda_0 = 0.06$ (except a, b, c), $\alpha_0 = 4$ (except d, e, f), $\kappa_0/k_0 = 0.34$ (except g, h, i), $\kappa_1/k_0 = 3.4$, $k_0 a_0 = 7.4$, $\psi_0 = \pi/3$ rad, $N_m = 34$, $z_0/\lambda_0 = 18$. Note the different vertical scale in (a, b, c). The SA and SA0 data in (f) and (i) overlap and therefore are not distinguishable. (For interpretation of the references to colour in this figure legend, the reader is referred to the web version of this article.)

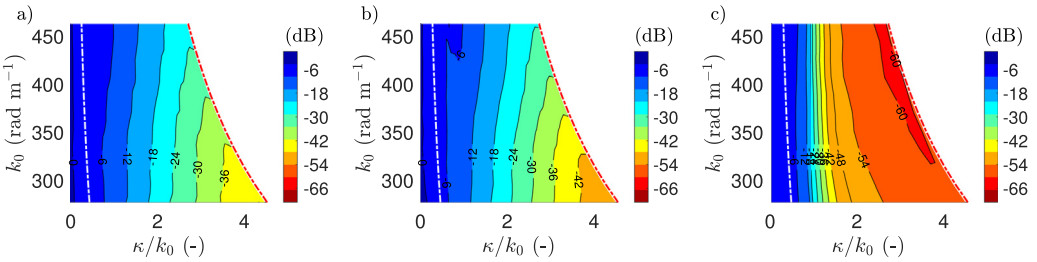

Fig. 10. Effect of the signal frequency on the reconstruction accuracy at various surface scales. Contour levels indicate the average ratio (in dB) between the Fourier power spectral densities of the target and reconstructed surface. The white and the red dash-dotted lines indicate the characteristic surface scale κ_0/k_0 and the shortest surface scale κ_1/k_0, respectively. SA (a), SA0 (b), and SP (c). Results are shown for $\alpha_0 = 4$, $k_0 a_0 = 7.4$, $\psi_0 = \pi/3$ rad, $N_m = 34$. (For interpretation of the references to colour in this figure legend, the reader is referred to the web version of this article.)

3.7. Frequency dependence

To explore the hypothesis of the inversion procedure acting as a low-pass filter of the surface, the power spectral density spectrum of the reconstructed surfaces was calculated, and compared with that of the known target surfaces, also exemplified by Eq. (26). The average (across multiple realizations) reconstructed/target ratio between these two spectra is shown in Fig. 10 as a function of the non-dimensionalized surface wavenumber κ/k_0, for various k_0. All three methods showed a tendency to underestimate the amplitude of the spectrum, by an amount that increased consistently with the normalized surface wavenumber κ/k_0, almost independently of the absolute value of k_0. In particular, scales shorter than $\approx 2\lambda_0$ had their power spectral density underestimated in average by more than 6 dB, for all methods. This underestimation increased even faster for the SP method, which appeared to be less sensitive to short wavelengths.

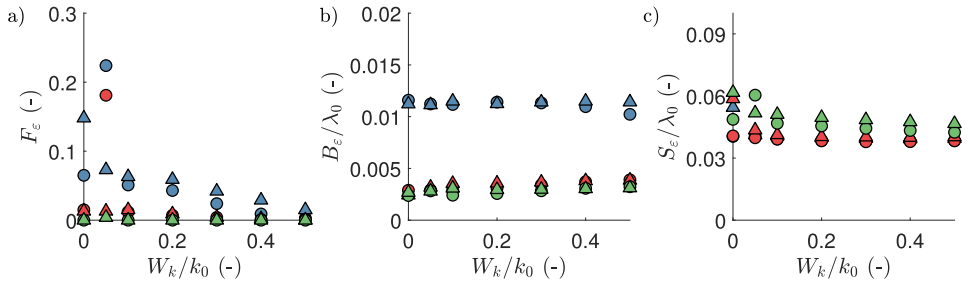

Fig. 11. Effect of the signal bandwidth W_k on the reconstruction error based on the multiple frequency extension of the SA (blue), SA0 (red), and SP (green) methods. Signal without noise (circles) and signal with 5% amplitude and phase noise (triangles). Results shown for $\sigma/\lambda_0 = 0.06$, $\alpha_0 = 4$, $\kappa_0/k_0 = 0.34$, $\kappa_1/k_0 = 3.4$, $k_0 a_0 = 7.4$, $\psi_0 = \pi/3$ rad, $N_m = 34$, $z_0/\lambda_0 = 18$. (For interpretation of the references to colour in this figure legend, the reader is referred to the web version of this article.)

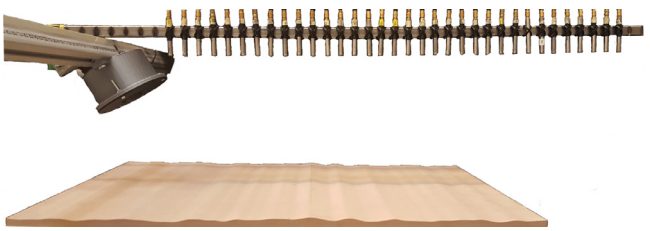

Fig. 12. A photograph of the experimental setup.

3.8. Multiple frequency extension

All results so far were obtained using the signal at a single frequency f_0. The outcome of considering multiple frequencies simultaneously according to the method described in Section 2 is presented in Fig. 11. Here, the reconstruction was based on a discrete set of wavenumbers $k_1, k_2, \ldots, k_{N_k}$, where $W_k = k_{N_k} - k_1$ was the effective bandwidth, the wavenumber grid spacing was set as $W_k/(N_k - 1) = 0.0025 k_0$, and the center wavenumber was $k_0 = \sum_j k_j/N_k$. The error metrics were evaluated for W_k/k_0 between 0 (single frequency case) and 0.5, without noise and with 5% amplitude and phase uncertainty. All results shown in Fig. 11 were obtained with a fixed number of microphones, $N_m = 34$, and of reconstruction points, $N_r = 991$, while the number of frequency bands was $N_k = 400 W_k/k_0 + 1$ and varied between 1 and 201. As a result, the ratio between number of rows and number of columns of the transfer matrix, $N_m N_k/N_r$ varied between 0.03 (single frequency case) and 6.90. A ratio $N_m N_k/N_r = 1$, which indicates the transition from an underdetermined to an overdetermined problem, would have been obtained with $W_k/k_0 = 0.073$. As seen in Fig. 11, the increase of the bandwidth caused a slight decrease of S_ε/λ_0 for all methods, and a slight increase of the bias B_ε/λ_0 for the SA0 and SP methods. The improvement in S_ε/λ_0 was larger in the presence of noise, and did not increase further beyond $W_k/k_0 = 0.1$ ($N_m N_k/N_r = 1.4$). Widening the bandwidth generally reduced the probability of failure F_ε, more visibly in the presence of noise. Without noise, F_ε initially showed a peak at $W_k/k_0 = 0.05$. For this case, $N_m N_k/N_r = 0.7$, meaning that the problem was still underdetermined and required solution via a singular value decomposition. The presence of a peak of F_ε only for the case without noise suggests that the extended matrix was nearly singular without noise and with small broadband. For larger W_k/k_0, the problem was overdetermined, and the inversion was obtained with an iterative least squares procedure [52]. The steep decline of F_ε for larger W_k/k_0, observed in Fig. 11, suggests that the least squares inversion is more robust.

4. Experimental validation

4.1. Experimental setup

Experimental tests were performed using an array of 34 1/4" microphones (G.R.A.S. 40PH) and a loudspeaker (Visaton G 25 FFL) positioned above a set of two rigid rough surfaces with known profiles (Fig. 12). The surfaces were milled on one side of two tiles made of medium density fiberboard (MDF) and aluminum, respectively. The opposite side of the tiles was flat. The MDF surface had a power-function spectrum like the one described by Eq. (26), with $\sigma_0 = 1$ mm, $\alpha_0 = 5$, $\kappa_0 = 2\pi/0.05$ rad m^{-1}, $\kappa_1 = 2\pi/0.01$ rad m^{-1}, and had dimensions of 0.6×0.4 m^2. Being asymmetric and aperiodic, this surface could be tested twice after a 180° rotation, effectively yielding two different surfaces with similar properties (surface A and B, Fig. 13d and e, in black). The aluminum surface had the shape of a sinusoid with wavelength 50 mm and peak-to-peak amplitude of 3 mm (surface C, Fig. 13f, in black).

For the experiments, the speaker was mounted at a height $z_0 = 230$ mm, and with an angle of 60°. The directivity of the speaker was measured, and the equivalent radius was estimated as approximately $a_0 = 20$ mm. The spacing between

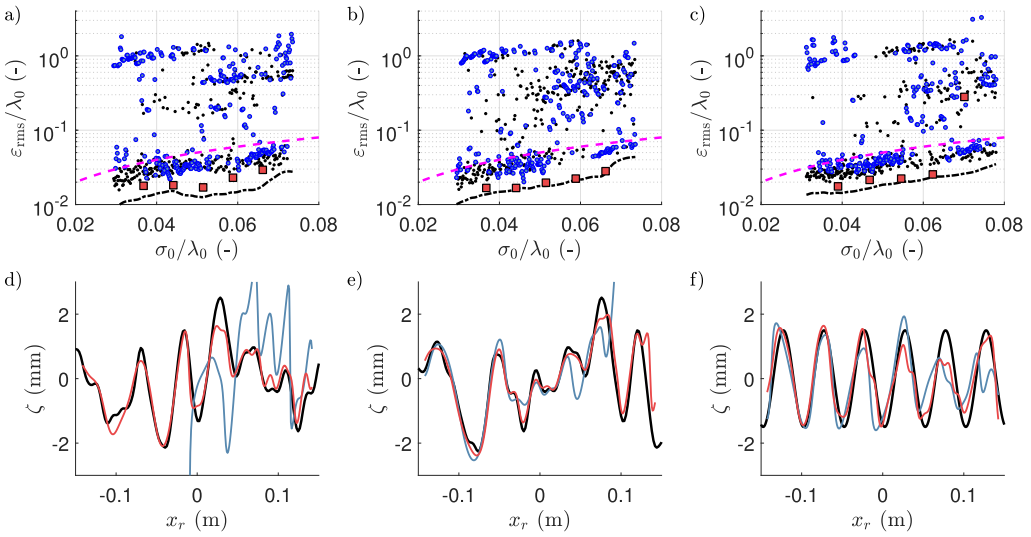

Fig. 13. Surface shape reconstruction using experimental data. Surfaces A (a, d), B (b, e), and C (c, f). (a, b, and c): non-dimensionalised rms-averaged local reconstruction error, for various acoustic frequencies and for three different surfaces. All results shown were obtained with the SA0 method and its broadband extension. (●) : reconstruction based on experimental data; (- · - · -): reconstruction based on synthetic data, without noise; (●): reconstruction based on synthetic data, with 5% amplitude and phase noise; (■): reconstruction obtained with the multiple frequencies extension with bandwidth $W_k =$ 148 rad m^{-1} and center frequency shown at the abscissa; (- - - -): $\varepsilon_{\mathrm{rms}} = \sigma_0$. (d, e, and f): examples of surface reconstruction. (———): target 'known' surface geometry; (———) : reconstruction based on experimental data at 17.5 kHz ($\sigma_0/\lambda_0 = 0.05$); (———): reconstruction obtained with the multiple frequencies extension with $f_0 = 17.5$ kHz, $W_k/k_0 = 0.46$.

microphones was 20 mm. The experimental setup differed slightly from the simplified model described thus far, in that the microphones were higher than the speaker, $z_m = 295$ mm. This was chosen to minimize the direct field. The overall length of the array was 660 mm, and the effective reconstruction domain had size $\Lambda = 284$ mm.

The speaker was energized with both single frequency harmonic signals and with a random white noise with higher cut-off frequency of 51.2 kHz. The signals were recorded at a frequency of 102.4 kHz. The complex amplitude of the recorded signal was calculated by means of a Fourier transform with a segment duration of 0.02 s, the result was divided by the transform of the input signal to remove the time-dependence, and then averaged over 40 s with no overlap. No significant difference between the measurements with harmonic signals and those obtained at the same frequency by a Fourier transform of the white noise were observed. All results presented here have been obtained from the white noise, by selecting only the frequencies of interest from the wider spectrum.

Calibration of each microphone in amplitude and phase was performed in situ, as follows: (i) the sound field reflected by a flat surface (the flat side of each tile) was recorded, and denoted as $\tilde{P}_0(\mathbf{M}_m, k)$; (ii) the same flat-surface reflection was calculated with Eq. (3), based on the known position of the speaker and microphones, and denoted as $P_0(\mathbf{M}_m, k)$; (iii) a frequency-dependent calibration factor was calculated for each microphone as $\mathcal{C}(\mathbf{M}_m, k) = P_0(\mathbf{M}_m, k)/\tilde{P}_0(\mathbf{M}_m, k)$. Every subsequent measurement obtained with the rough surfaces (after turning the tile upside down) was corrected by means of a multiplication by the complex factor $\mathcal{C}(\mathbf{M}_m, k)$. Numerical simulations were performed alongside each experimental test using the known setup and surface geometry as input, to aid the interpretation of the results.

4.2. Experimental results

The results of the experimental tests obtained with the SA0 method are exemplified in Fig. 13. The SA0 method was chosen because it was expected to yield the best results according to the numerical analysis in Section 3. The single-frequency reconstruction was performed independently at frequencies ranging between 10 kHz and 25 kHz. This corresponds to values of σ_0/λ_0 between 0.03 and 0.07. Since only three surfaces were tested, a statistical analysis of the reconstruction error was not possible, and the three error metrics defined in Section 3 could not be calculated. Instead, the reconstruction error was quantified in terms of the rms spatial average of the local difference $\varepsilon(x_r) = \tilde{\zeta}(x_r) - \zeta(x_r)$ over the effective reconstruction domain. These errors are shown in Fig. 13a–c with blue dots, for the experimental data.

With this definition, the error in the single-frequency reconstruction exhibits a strong sensitivity to the operational frequency. The target surface profiles are shown in black in Figs. 13d, e, and f for surfaces A, B and C, respectively. An example of monochromatic reconstruction, obtained at a frequency of 17.5 kHz ($\sigma_0/\lambda_0 = 0.05$), is shown in blue in the same figures. The monochromatic reconstruction is reasonably close to the actual surface shape for surfaces B and C (Fig. 13e and f), while little resemblance to the target was found for surface A (Fig. 13d) at this frequency. For the case shown in Fig. 13d, e, and f, the measured relative errors $\varepsilon_{\mathrm{rms}}/\lambda_0$ were 0.44 (surface A), 0.27 (surface B), and 0.038 (surface C). The percentage

of frequencies (relative to all tested frequencies shown in Fig. 13a–c) that had a relative reconstruction error larger than 0.1 was 46% for Surface A, 40% for Surface B, and 50% for Surface C. These percentages can be assumed to be indicative of an equivalent probability of failure of the reconstruction. The reconstruction in Fig. 13d (surface A) is one typical example of such failure, but also in Fig. 13e the large rms error is due to the strong departure from the target profile near $x_r = 0.1$ m. Excluding the obvious failures, the relative error $\varepsilon_{\mathrm{rms}}/\lambda_0$ was found increasing with σ_0/λ_0, as expected, and was generally between 0.03 and 0.06, or between 60% and 80% of σ_0/λ_0. The limiting condition $\varepsilon_{\mathrm{rms}}/\sigma_0 = 1$ is shown in Fig. 13a–c with a purple dashed line. To determine if these figures were in line with the expectations, the reconstruction was applied to synthetic signals obtained based on the same known surface profiles. The expected values of $\varepsilon_{\mathrm{rms}}/\lambda_0$ calculated without artificial noise ($\sigma_\xi = \sigma_\chi = 0$) are indicated with a dashed line in Fig. 13a–c, and were considerably smaller, at ≈ 0.02, or between 30% and 40% of σ_0/λ_0. The addition of 5% uncertainty to the amplitude and phase of the synthetic signal yielded values more in line with the measurements, also bringing the failure rate to between 38% (surface B) and 63% (surface A). The 'noisy' synthetic data points are indicated with black dots in Fig. 13a–c and show a sensitivity to frequency similar to that of the experimental cases.

Given the choice of acoustic stimulus used for the measurement (white noise), data at multiple frequencies was easily collected simultaneously for the three surfaces. This data was analyzed with the multiple frequency extension of the SA0 method, selecting portions of the overall signal spectrum with a constant bandwidth of $W_k = 148$ rad m^{-1} (6 kHz), and a range of different center frequencies from 12.5 kHz to 22.5 kHz. The corresponding rms errors are shown with red rectangles in Fig. 13a–c, for each center frequency. Examples of reconstruction obtained with a center frequency of 17.5 kHz ($\sigma_0/\lambda_0 = 0.05$) are also shown in red in Fig. 13d–f. Compared to the single frequency reconstruction (blue line), the multiple frequency reconstruction appeared closer to the known surface profile. The measured relative rms errors for a center frequency of 17.5 kHz were 0.017 (surface A), 0.020 (surface B), and 0.022 (surface C), corresponding to 33%, 38%, and 41% of σ_0. Unlike the single frequency case, the reconstruction was similarly accurate for all three surfaces, and the error varied less with the center frequency. Even with the multiple frequency extension, however, the probability of failure of the reconstruction was not zero, as revealed by the large rms error observed in Fig. 13c for surface C, at $\sigma_0/\lambda_0 = 0.07$. However, all remaining cases showed errors close to the theoretical limit, represented here by the synthetic results without noise.

The results obtained with the SA and SP methods (not shown in Fig. 13) mostly confirmed the results obtained in Section 3 with synthetic data. In the single-frequency case, reconstruction errors larger than $0.1\lambda_0$ were observed at between 72% and 84% of frequencies (between 64% and 80% with synthetic noisy data) for the SA method, and at between 32% and 43% of frequencies (between 9% and 18% with synthetic noisy data) for the SP method, which confirms a lack of robustness of the SA method. The relative error $\varepsilon_{\mathrm{rms}}/\lambda_0$ at the center frequency of 17.5 kHz was found to vary between 0.09 and 0.49 for the measurements with the SA method (between 0.16 and 0.37 with synthetic data), and between 0.033 and 0.067 for the measurements with the SP method (between 0.028 and 0.048 with synthetic data). Note that for the three surfaces that were tested here, $\sigma_0/\lambda_0 < 0.1$, which was within the range where the performance of the SP and SA0 method were expected to be comparable (see Fig. 9a–c). For the SP method, the multiple frequency extension effectively reduced the relative error to values between 0.02 and 0.03, close to the theoretical limit. For the SA method, the multiple-frequency reconstruction error decreased substantially for surface A (approximately 0.02), while it remained relatively large for surface B (between 0.03 and 0.1) and for surface C (between 0.03 and 0.08). For both surfaces, the largest errors were observed at the highest frequencies.

5. Discussion

The numerical results presented in Section 3 suggested overall better performance of the SA0 method compared to the SA and SP alternatives, for the cases considered here. The SA0 method was less affected by bias at small σ_0/λ_0 compared to SA, and had smaller deviation S_ε/λ_0 than the SP method at large σ_0/λ_0. A possible explanation for the bias of the SA method at small σ_0/λ_0 can be identified in the regularization of the inverse problem in the sense of Tikhonov. The solution obtained by means of the Tikhonov regularization minimizes a weighted sum of the inversion residual and of the norm of the solution itself [46]. The latter is represented here by the vector **E**. However, for the SA method, a solution that minimizes the norm of **E** does not minimize ζ. This could explain the bias at low σ_0/λ_0, when the regularization is expected to have a stronger impact due to the smaller sensitivity of the scattered field. By removing the bias of the solution vector **E**, the SA0 method effectively restores the applicability of the Tikhonov regularization, thus improving the performance of the reconstruction. The relative weight of the two norms minimized by the Tikhonov regularization is governed by the regularization parameter, which was determined here by means of the generalized cross-validation method. It is possible that further improvements could be obtained by means of alternative regularization approaches. These should be evaluated in future studies, using the error analysis framework introduced here.

Amongst all parameters that affect the accuracy of the reconstruction, the relative roughness standard deviation σ_0/λ_0 had the strongest influence. Considering the SA0 method, lower σ_0/λ_0 was associated with smaller values of all three error metrics. However, at $\sigma_0/\lambda_0 < 0.1$, the deviation S_ε was found very close to σ_0. This would be unacceptable in most cases, since the uncertainty needs to be considerably lower than the characteristic amplitude of roughness. To increase the ratio S_ε/σ_0, one would need to increase the frequency of the signal (hence σ_0/λ_0). This would also improve the ability to reconstruct shorter scales on the surface, as shown with Fig. 10, but it would in turn increase very rapidly the probability of

failure. The quality of the reconstruction must rely on a compromise between accuracy and robustness, which is often made even more difficult by a lack of prior knowledge about the surface properties.

The severity of the robustness issue was highlighted by the experimental results shown in Fig. 13. Here, a relatively small amount of noise in the data was shown making the reconstruction fail for more than 40% of the cases, for a given surface, merely because of the different frequency used for the analysis. This is of notice, especially since the theoretical probability of failure for the same surfaces, without noise, was close to zero, as shown by the numerical simulations. A multiple-frequency extension applicable to all methods was here proposed as a possible solution to maintain accuracy and improve robustness. With synthetic data, the impact of the extension on the analysis was somehow limited, although a substantial decrease of the probability of failure was demonstrated for the SA method in presence of noise. When applied to the experimental data, the extension gave results that were considerably more reliable and accurate than any single-frequency reconstruction, with an accuracy close to the theoretical limit calculated numerically.

6. Conclusions

This work provided a systematic comparison of various approaches to reconstruct a rough surface from measurements of the scattered acoustic field with a linear array of microphones. For all approaches, and for the range of conditions examined in this work, the linearization of the scattering equations proposed in [17] was found having a small effect on the reconstruction error. Instead, large errors were found arising from the inversion itself, likely as a result of the underdetermined and ill-posed nature of the problem. The reconstruction error was found to be strongly influenced by the ratio between roughness height and acoustic wavelength. Accuracy and resolution were found to improve at higher frequencies, at the expense of robustness.

One of the new approaches proposed here, which addresses an inconsistent use of the Tikhonov regularization in [17] by introducing a pre-conditioning of the problem, was found giving the best overall results. A further improvement was introduced via a multiple-frequency extension of the reconstruction procedure, which allows to combine information at multiple frequencies into a single, potentially overdetermined, linear problem. Application of this extended approach to the experimental data collected simultaneously over a broad range of frequencies, using a white noise as stimulus, demonstrated its efficacy in improving the robustness and reliability of the reconstruction, while providing errors close to the theoretical limit for the three tested surfaces.

The main advantage of the surface reconstruction methodology under exam is its capability to estimate the surface shape using a relatively small number of sensors. This makes the technique fast, inexpensive, and simple to set up, calibrate, and operate. Although the method is derived for acoustic waves interacting with a sound-rigid surface, the extension to electromagnetic waves and/or Dirichlet boundary conditions should be feasible. Application to surfaces with larger or smaller scales should be possible as long as all quantities including the signal frequency are scaled consistently, and the Kirchhoff approximation can be assumed valid. The results presented here can inform the design of measurement arrays for a variety of potential applications, while providing an indication of the limitations and uncertainties of the method.

Declaration of Competing Interest

The authors declare that they have no known competing financial interests or personal relationships that could have appeared to influence the work reported in this paper.

CRediT authorship contribution statement

G. Dolcetti: Conceptualization, Methodology, Software, Investigation, Writing - original draft, Visualization. **M. Alkmim:** Investigation, Data curation, Writing - review & editing. **J. Cuenca:** Investigation, Resources, Writing - review & editing. **L. De Ryck:** Investigation, Resources, Writing - review & editing. **A. Krynkin:** Conceptualization, Methodology, Writing - review & editing, Project administration, Funding acquisition.

Acknowledgments

The Matlab scripts used to calculate the Kirchhoff acoustic potential and reconstruct the surface shape are available online at the following link: https://doi.org/10.5281/zenodo.3958859 [47]. The authors are grateful to P. Bonfiglio (Materiacustica srl) for suggesting the in-situ calibration procedure. This work was supported by Knowledge Exchange Support Fund provided by the UK Engineering and Physical Sciences Research Council (EPSRC). G. Dolcetti is funded by the UK EPSRC Grant EP/R022275/1. M. Alkmim is funded by the Marie Sklodowska Curie program through the H2020 ETN PBNv2 project (GA 721615).

Appendix A. Kirchhoff approximation for a cylindric surface

Consider scattering of sound with wavenumber k generated by a point source with co-ordinates $\mathbf{S}$, scattered by a rough surface $z = \zeta(x, y)$, and recorded at location $\mathbf{M}_m$. A point on the surface is identified by the vector $\boldsymbol{\rho} = (x, y, \zeta(x, y))$. As-

suming the validity of the Kirchhoff approximation, the complex potential at $\mathbf{M}_m$ is [41, p. 226–228]

$$P(\mathbf{M}_m, k) = 4\pi \iint \mathbf{n} \cdot \nabla[P_i(\mathbf{S}, \boldsymbol{\rho}, k) G_0(\mathbf{M}_m, \boldsymbol{\rho}, k)] \frac{\mathrm{d}x\mathrm{d}y}{\sqrt{1 + |\nabla\zeta|^2}}, \tag{A.1}$$

where the term inside the square root in Eq. (A.1) arises by changing variable of integration from the curvilinear surface-following variable to the Cartesian variables x and y. $\mathbf{n}$ is the unit vector normal to the surface, G_0 is the far-field Green's function,

$$G_0(\mathbf{r}, \mathbf{r}') = -\frac{1}{4\pi} \frac{\mathrm{e}^{\mathrm{i}k|\mathbf{r}'-\mathbf{r}|}}{|\mathbf{r}' - \mathbf{r}|}, \tag{A.2}$$

P_i is the incident field,

$$P_i(\mathbf{S}, \boldsymbol{\rho}, k) = p_0 \mathrm{e}^{-\mathrm{i}2\pi f t} \frac{D(\theta(\boldsymbol{\rho} - \mathbf{S}))}{k} G_0(\mathbf{S}, \boldsymbol{\rho}), \tag{A.3}$$

t is time, and p_0 is the signal amplitude, which carries the dimensions of an acoustic potential. Without loss of generality, hereafter it is assumed $p_0 e^{-\mathrm{i}2\pi f t} = 1$, so that $P(\mathbf{M}_m, k_0)$ takes the meaning of a normalized complex Fourier coefficient.

Substituting Eqs. (A.2) and (A.3) into Eq. (A.1), assuming a slowly varying directivity, yields an equation of the form

$$P(\mathbf{M}_m, k) = \iint \mathcal{C}(\mathbf{S}, \mathbf{M}_m, \boldsymbol{\rho}, k) \exp\{\mathrm{i}k[|\boldsymbol{\rho} - \mathbf{S}| + |\mathbf{M}_m - \boldsymbol{\rho}|]\} \mathrm{d}x\mathrm{d}y, \tag{A.4}$$

where

$$\begin{aligned} \mathcal{C}(\mathbf{S}, \mathbf{M}_m, \boldsymbol{\rho}, k) = {} & \frac{\mathrm{i}}{4\pi} \frac{D(\theta(\boldsymbol{\rho} - \mathbf{S}))}{|\boldsymbol{\rho} - \mathbf{S}||\mathbf{M}_m - \boldsymbol{\rho}|} \\ & \times \left\{ \left[1 + \frac{\mathrm{i}}{k|\boldsymbol{\rho} - \mathbf{S}|} \right] \left[-\frac{(x - x_s)}{|\boldsymbol{\rho} - \mathbf{S}|} \frac{\partial\zeta}{\partial x} - \frac{(y - y_s)}{|\boldsymbol{\rho} - \mathbf{S}|} \frac{\partial\zeta}{\partial y} + \frac{(\zeta - z_s)}{|\boldsymbol{\rho} - \mathbf{S}|} \right] \right. \\ & \left. + \left[1 + \frac{\mathrm{i}}{k|\mathbf{M}_m - \boldsymbol{\rho}|} \right] \left[-\frac{(x - x_m)}{|\mathbf{M}_m - \boldsymbol{\rho}|} \frac{\partial\zeta}{\partial x} - \frac{(y - y_m)}{|\mathbf{M}_m - \boldsymbol{\rho}|} \frac{\partial\zeta}{\partial y} + \frac{(\zeta - z_m)}{|\mathbf{M}_m - \boldsymbol{\rho}|} \right] \right\}. \end{aligned} \tag{A.5}$$

The source and microphone are assumed to lie on the x–z plane, $y_m = y_s = 0$. Assuming no variation of ζ along y, $\partial\zeta/\partial y = 0$, then the complex exponential in Eq. (A.4) has a stationary phase point at $y = 0$. Applying a stationary phase expansion [e.g., 53, ch. 6.5, p. 276], and integrating along y, yields

$$P(\mathbf{M}_m, k) \approx \mathrm{e}^{\mathrm{i}\pi/4} \sqrt{\frac{2\pi}{k}} \int \sqrt{\frac{R(\mathbf{S}, \boldsymbol{\rho}_0) R(\mathbf{M}_m, \boldsymbol{\rho}_0)}{R(\mathbf{S}, \boldsymbol{\rho}_0) + R(\mathbf{M}_m, \boldsymbol{\rho}_0)}} \mathcal{C}(\mathbf{S}, \mathbf{M}_m, \boldsymbol{\rho}_0, k) \exp\{\mathrm{i}k[R(\mathbf{S}, \boldsymbol{\rho}_0) + R(\mathbf{M}_m, \boldsymbol{\rho}_0)]\} \mathrm{d}x, \tag{A.6}$$

where $\boldsymbol{\rho}_0 = (x, 0, \zeta(x))$. This leads to Eq. (3).

Supplementary material

Supplementary material associated with this article can be found, in the online version, at doi:10.1016/j.jsv.2020.115902.

References

[1] L. Hellequin, J.-M. Boucher, X. Lurton, Processing of high-frequency multibeam echo sounder data for seafloor characterization, IEEE J. Oceanic Eng. 28 (1) (2003) 78–89.
[2] J.T. Johnson, R.J. Burkholder, J.V. Toporkov, D.R. Lyzenga, W.J. Plant, A numerical study of the retrieval of sea surface height profiles from low grazing angle radar data, IEEE Trans. Geosci. Remote 47 (6) (2008) 1641–1650.
[3] S.P. Walstead, G.B. Deane, Reconstructing surface wave profiles from reflected acoustic pulses using multiple receivers, J. Acoust. Soc. Am. 136 (2) (2014) 604–613.
[4] A. Nichols, S. Tait, K. Horoshenkov, S. Shepherd, A non-invasive airborne wave monitor, Flow Meas. Instrum. 34 (2013) 118–126.
[5] G. Dolcetti, A. Krynkin, K.V. Horoshenkov, S.J. Tait, An acoustic technique to measure the velocity of shallow turbulent flows remotely, in: M. Kalinowska, M. Mrokowska, P. Rowinski (Eds.), Free Surface Flows and Transport Processes, GeoPlanet: Earth and Planetary Sciences, Springer, Cham, 2018, pp. 181–194.
[6] J.C. Quartel, C.J.R. Sheppard, Surface reconstruction using an algorithm based on confocal imaging, J. Mod. Optic. 43 (3) (1996) 469–486.
[7] D. Macías, E.R. Méndez, V. Ruiz-Cortés, Inverse scattering with a wave-front-matching algorithm, J. Opt. Soc. Am. A 19 (10) (2002) 2064–2073.
[8] R.J. Wombell, J.A. DeSanto, Reconstruction of rough-surface profiles with the Kirchhoff approximation, J. Opt. Soc. Am. A 8 (12) (1991) 1892–1897.
[9] S. Chandler-Wilde, C. Ross, Uniqueness results for direct and inverse scattering by infinite surfaces in a lossy medium, Inverse Probl. 11 (5) (1995) 1063.
[10] M. El-Shenawee, E.L. Miller, Multiple-incidence and multifrequency for profile reconstruction of random rough surfaces using the 3-D electromagnetic fast multipole model, IEEE Trans. Geosci. Remote 42 (11) (2004) 2499–2510.
[11] S. Afifi, M. Diaf, Scattering by random rough surfaces: study of direct and inverse problem, Opt. Commun. 265 (1) (2006) 11–17.
[12] I. Akduman, R. Kress, A. Yapar, Iterative reconstruction of dielectric rough surface profiles at fixed frequency, Inverse Probl. 22 (3) (2006) 939.
[13] Y. Chen, M. Spivack, Rough surface reconstruction at grazing angles by an iterated marching method, J. Opt. Soc. Am. A 35 (4) (2018) 504–513.
[14] H.-A. Diao, P. Li, X. Yuan, Inverse elastic surface scattering with far-field data, Inverse Probl. Imag. 13 (4) (2019) 721–744.
[15] R. Coifman, M. Goldberg, T. Hrycak, M. Israeli, V. Rokhlin, An improved operator expansion algorithm for direct and inverse scattering computations, Wave. Random Media 9 (3) (1999) 441–458.
[16] M. Stankova, J. Burov, M. Burova, Computer reconstruction of a periodic surface by means of the scattered and transmitted acoustic fields, Meas. Sci. Technol. 12 (8) (2001) 1330.

[17] A. Krynkin, K.V. Horoshenkov, T. Van Renterghem, An airborne acoustic method to reconstruct a dynamically rough flow surface, J. Acoust. Soc. Am. 140 (3) (2016) 2064–2073.
[18] G. Bao, L. Zhang, Uniqueness results for scattering and inverse scattering by infinite rough surfaces with tapered wave incidence, SIAM J. Imaging Sci. 11 (1) (2018) 361–375.
[19] Y. Zhao, G. Hu, B. Yan, Uniqueness to inverse acoustic and electromagnetic scattering from locally perturbed rough surfaces, Appl. Anal. (2019) 1–22.
[20] F. Qu, B. Zhang, H. Zhang, A novel integral equation for scattering by locally rough surfaces and application to the inverse problem: the Neumann case, SIAM J. Sci. Comput. 41 (6) (2019) A3673–A3702.
[21] V. Galdi, J. Pavlovich, W.C. Karl, D.A. Castañon, L.B. Felsen, Moderately rough dielectric interface profile reconstruction via short-pulse quasi-ray Gaussian beams, IEEE T. Antenn. Propag. 51 (3) (2003) 672–677.
[22] C. Burkard, R. Potthast, A time-domain probe method for three-dimensional rough surface reconstructions, Inverse Probl. Imag. 3 (2) (2009) 259–274.
[23] C.D. Lines, S.N. Chandler-Wilde, A time domain point source method for inverse scattering by rough surfaces, Computing 75 (2–3) (2005) 157–180.
[24] C. Burkard, R. Potthast, A multi-section approach for rough surface reconstruction via the Kirsch–Kress scheme, Inverse Probl. 26 (4) (2010) 045007.
[25] X. Liu, B. Zhang, H. Zhang, A direct imaging method for inverse scattering by unbounded rough surfaces, SIAM J. Imaging Sci. 11 (2) (2018) 1629–1650.
[26] R. Kress, T. Tran, Inverse scattering for a locally perturbed half-plane, Inverse Probl. 16 (5) (2000) 1541.
[27] V. Galdi, D.A. Castañon, L.B. Felsen, Multifrequency reconstruction of moderately rough interfaces via quasi-ray Gaussian beams, IEEE Trans. Geosci. Remote 40 (2) (2002) 453–460.
[28] H. Zhang, B. Zhang, A novel integral equation for scattering by locally rough surfaces and application to the inverse problem, SIAM J. Appl. Math. 73 (5) (2013) 1811–1829.
[29] Y.-Q. Jin, Z. Li, Reconstruction of roughness profile of fractal surface from scattering measurement at grazing incidence, J. Appl. Phys. 89 (3) (2001) 1922–1926.
[30] E. Kiliç, M. Çayören, A. Yapar, Í. Akduman, Reconstruction of perfectly conducting rough surfaces by the use of inhomogeneous surface impedance modeling, Inverse Probl. Imag. 3 (2) (2009) 295.
[31] M. Spivack, Direct solution of the inverse problem for rough surface scattering at grazing incidence, J. Phys. A 25 (11) (1992) 3295.
[32] M. Spivack, Solution of the inverse-scattering problem for grazing incidence upon a rough surface, J. Opt. Soc. Am. A 9 (8) (1992) 1352–1355.
[33] A. Schatzberg, A.J. Devaney, Rough surface inverse scattering within the Rytov approximation, J. Opt. Soc. Am. A 10 (5) (1993) 942–950.
[34] R. Wombell, J.A. DeSanto, The reconstruction of shallow rough-surface profiles from scattered field data, Inverse Probl. 7 (1) (1991) L7.
[35] W. Veronesi, J. Maynard, Digital holographic reconstruction of sources with arbitrarily shaped surfaces, J. Acoust. Soc. Am. 85 (2) (1989) 588–598.
[36] Q. Leclère, Acoustic imaging using under-determined inverse approaches: frequency limitations and optimal regularization, J. Sound Vib. 321 (3–5) (2009) 605–619.
[37] A. Krynkin, G. Dolcetti, S. Hunting, Acoustic imaging in application to reconstruction of rough rigid surface with airborne ultrasound waves, Rev. Sci. Instrum. 88 (2) (2017) 024901.
[38] J. Li, G. Sun, A nonlinear integral equation method for the inverse scattering problem by sound-soft rough surfaces, Inverse Probl. Sci. Eng. 23 (4) (2015) 557–577.
[39] F. Le Louër, M.-L. Rapún, Detection of multiple impedance obstacles by non-iterative topological gradient based methods, J. Comput. Phys. 388 (2019) 534–560.
[40] E.I. Thorsos, The validity of the Kirchhoff approximation for rough surface scattering using a Gaussian roughness spectrum, J. Acoust. Soc. Am. 83 (1) (1988) 78–92.
[41] F.G. Bass, I.M. Fuks, Wave Scattering from Statistically Rough Surfaces, vol. 93, Oxford Pergamon, Oxford, UK, 1979.
[42] G. Dolcetti, A. Krynkin, Doppler spectra of airborne ultrasound forward scattered by the rough surface of open channel turbulent water flows, J. Acoust. Soc. Am. 142 (5) (2017) 3122–3134.
[43] G. Dolcetti, A. Krynkin, K.V. Horoshenkov, Doppler spectra of airborne sound backscattered by the free surface of a shallow turbulent water flow, J. Acoust. Soc. Am. 142 (6) (2017) 3387–3401.
[44] W.H. Press, S.A. Teukolsky, W.T. Vetterling, B.P. Flannery, Numerical Recipes 3rd Edition: The Art of Scientific Computing, Cambridge University Press, Cambridge, 2007.
[45] G.H. Golub, M. Heath, G. Wahba, Generalized cross-validation as a method for choosing a good ridge parameter, Technometrics 21 (2) (1979) 215–223.
[46] P.C. Hansen, Regularization tools: A Matlab package for analysis and solution of discrete ill-posed problems, Numer. Algorithms 6 (1) (1994) 1–35.
[47] G. Dolcetti, A. Krynkin, Matlab codes for two-dimensional scattering surface reconstruction using broadband acoustic data, 2020. doi:10.5281/zenodo.3958859.
[48] P.M. Morse, K.U. Ingard, Theoretical Acoustics, Princeton University Press, 1986.
[49] O.M. Phillips, The equilibrium range in the spectrum of wind-generated waves, J. Fluid Mech. 4 (4) (1958) 426–434.
[50] D.R. Jackson, D.P. Winebrenner, A. Ishimaru, Application of the composite roughness model to high-frequency bottom backscattering, J. Acoust. Soc. Am. 79 (5) (1986) 1410–1422.
[51] M.T. Stewart, S.M. Cameron, V.I. Nikora, A. Zampiron, I. Marusic, Hydraulic resistance in open-channel flows over self-affine rough beds, J. Hydraul. Res. 57 (2) (2019) 183–196.
[52] C.C. Paige, M.A. Saunders, LSQR: An algorithm for sparse linear equations and sparse least squares, ACM Trans. Math. Softw. 8 (1) (1982) 43–71.
[53] C.M. Bender, S.A. Orszag, Advanced Mathematical Methods for Scientists and Engineers I: Asymptotic Methods and Perturbation Theory, Springer Science & Business Media, 2013.